

To appear in Ap. J.

Multi-epoch Imaging Polarimetry of the SiO Masers in the Extended Atmosphere of the Mira Variable TX Cam

Athol J. Kemball

*Department of Astronomy, and
Institute for Advanced Computing Applications and Technologies
University of Illinois, 1002 W. Green Street, Urbana, IL 61801*

akemball@illinois.edu

Philip J. Diamond

*Jodrell Bank Center for Astrophysics
University of Manchester, Manchester, M13 9PL, United Kingdom*

philip.diamond@manchester.ac.uk

Ioannis Gonidakis

*Department of Astrophysics, Astronomy, & Mechanics,
University of Athens, GR-157 83, Athens, Greece*

gonidakis@gmail.com

and

Modhurita Mitra, Kijeong Yim, Kuo-Chuan Pan, and Hsin-Fang Chiang

*Department of Astronomy
University of Illinois, 1002 W. Green Street, Urbana, IL 61801*

ABSTRACT

We present a time series of synoptic images of the linearly-polarized $v = 1$, $J = 1 - 0$ SiO maser emission toward the Mira variable, TX Cam. These data comprise 43 individual epochs at an approximate biweekly sampling over an optical pulsation phase range of $\phi = 0.68$ to $\phi = 1.82$. The images have an angular resolution of $\sim 500\mu\text{as}$ and were obtained using the Very Long Baseline Array

(VLBA), operating in the 43 GHz band in spectral-line, polarization mode. We have previously published the total intensity time series for this pulsation phase range; this paper serves to present the linearly-polarized image sequence and an associated animation representing the evolution of the linear polarization morphology over time. We find a predominantly tangential polarization morphology, a high degree of persistence in linear polarization properties over individual component lifetimes, and stronger linear polarization in the inner projected shell than at larger projected shell radii. We present an initial polarization proper motion analysis examining the possible dynamical influence of magnetic fields in component motions in the extended atmospheres of late-type, evolved stars.

Subject headings: masers - polarization - stars: magnetic fields - stars: individual (TX Cam)

1. Introduction

The extended atmospheres of late-type, evolved stars on the asymptotic giant branch (AGB) are host to complex underlying astrophysical processes of vital importance. Mass-loss from these stars originates in this region and is an important enrichment mechanism for the interstellar medium. The large-amplitude, long-period variables (LALPV) span a range of variability sub-classes, including the Mira variables, with a median pulsation period of several hundred days (Habing 1996). Their near-circumstellar environments (NCSE) are permeated by pulsation shocks from the central star (Hinkle, Hall, & Ridgway 1982; Hinkle, Lebzelter, & Scharlach 1997; Alvarez et al. 2000) and complex convective motions in the outer envelope (Porter, Anderson, & Woodward 1997; Freytag, Steffen, & Dorch 2002). These stars have significant mass-loss rates and are often obscured in visible optical bands. SiO masers at 43 GHz are however ubiquitous in the extended atmospheres of these objects. As compact high-brightness components that are significantly polarized, they act as important probes of the astrophysics in the close circumstellar environment, including the morphology and relative dynamical influence of magnetic fields. Spectral-line polarization VLBI techniques allow direct imaging of this region in Stokes (I, Q, U, V) at a spatial resolution of μas , unmatched at other wave-bands. The power of this technique is significantly enhanced if synoptic monitoring is conducted over a range of stellar pulsation phase, so that the key dynamical drivers can be studied in this region.

There remain significant uncertainties in integrated astrophysical models of the NCSE. Stellar pulsation hydrodynamical models are either semi-analytic (Bertshinger & Chevalier 1985), or confined to spherical or axi-symmetric numerical studies (Bowen 1988; Bessell, Scholz & Wood

1996; Humphreys et al. 2002). Theoretical studies of magnetic fields in AGB stars have produced a range of predicted magnetic field magnitudes and morphologies. Blackman *et al.* (2001) have proposed a conventional $\alpha\omega$ dynamo driven by an inner, differentially-rotating stellar core. Photospheric fields of the order of ~ 400 G are predicted in this model, but for the case of an isolated (non-binary) AGB star, this model would need a dynamo re-supply mechanism to sustain a magnetic field for long enough to shape global mass loss (Nordhaus, Blackman, & Frank 2007). The role of magnetic fields in shaping the global mass-loss process is considered by (García-Segura et al. 1999). In contrast, a convective $\alpha^2\omega$ dynamo has been proposed by Soker & Zoabi (2002); in this model, turbulent dynamo fields may produce magnetic cool spots ($\sim 10 - 100$ G) that regulate local dust formation, but have no global shaping role in mass-loss (Soker 2002). Broader arguments against the proposition that global magnetic fields can shape planetary nebulae are summarized by Soker (2006). In a numerical MHD study, Dorch (2004) have examined a convective dynamo in a supergiant atmosphere and report predicted local fields of up to ~ 500 G. These fields would have significant dynamical influence, albeit localized with low filling factors.

Recent water maser polarimetry of late-type, evolved stars has found evidence for $> 10^2$ mG magnetic fields at the shell radius of the H_2O masers; this extrapolates to a surface field of $\sim 10^2$ G (Vlemmings, van Langevelde, & Diamond 2005). Recent optical spectroscopy of unobscured central stars in planetary nebulae (PNe) has measured photospheric magnetic fields of several kG in these stars (Jordan, Werner, & O’Toole 2005). Magnetic fields of this magnitude would be dynamically significant and of great astrophysical importance to related studies of collimation mechanisms for PPN (Meixner *et al.* 2004). A small subset of stellar water maser sources that show linear jets also appear to be magnetically collimated (Vlemmings, Diamond, & Imai 2006).

As part of a synoptic monitoring campaign of the $J = 1 - 0$ SiO maser emission toward the Mira variable TX Cam at fine time-sampling, this paper presents linear polarization images for the first 43 epochs observed, over a pulsation phase range $\phi = 0.68$ to $\phi = 1.82$. The reduction and analysis of the corresponding total intensity data was published earlier by Diamond & Kemball (2003, hereafter Paper I). This paper serves to present the time-series of linear polarization images, and provides an analysis of the linear polarization morphology and early results on associated proper motions. The associated circular polarization data will be presented in a future paper. TX Cam is an M8-M10 Mira variable with a pulsation period of 557.4 days (Kholopov et al. 1985), and has a Mira period-luminosity distance estimate of ~ 390 pc (Olivier, Whitelock, & Marang 2001). It was first observed in total intensity VLBI observations by Diamond et al. (1994). Recent simultaneous total intensity VLBI imaging of the $v = \{1, 2\}$, $J = 1 - 0$ transitions is reported by Yi *et al.* (2005).

The first polarimetric VLBI imaging of the $v = 1$, $J = 1 - 0$ SiO maser emission toward TX Cam was conducted at a single epoch by Kemball & Diamond (1997), who found a predominant orientation of the electric vector position angle (EVPA) tangent to the arc of the projected maser shell. This will be referred to as tangential polarization in what follows. Subsequent SiO VLBI imaging polarimetry of TX Cam and IRC+10011 at a later single epoch was carried out by Desmurs *et al.* (2000), who found a similar tangential linear polarization morphology. A combined optical interferometric and VLBI polarimetric monitoring campaign for a sample of O-rich AGB stars, but not including TX Cam, is currently underway and is described in a series of papers by Cotton *et al.* (2004), Cotton *et al.* (2006), and Cotton, Perrin, & Lopez (2008). Recent single-dish polarimetry of the SiO $J = 2 - 1$ transition at 86 GHz for a sample of late-type, evolved stars is reported by Herpin *et al.* (2006).

The structure of this paper is as follows. Section 2 describes the observations and data reduction methods. The results and discussion are presented in Section 3, and conclusions in Section 4.

2. Observations and Data Reduction

In this paper we present the polarization reduction of the time-series of 43 synoptic observations of the $v = 1$, $J = 1 - 0$ SiO maser emission toward TX Cam, previously analyzed and reported in total intensity in Paper I. The list of epoch codes, observing dates, and associated TX Cam optical pulsation phases are repeated here for reference as Table 1. The observations in this paper cover the time interval from 24 May 1997 to 19 February 1999, corresponding to a TX Cam pulsation phase range $\phi = 0.68$ to $\phi = 1.82$. The data were observed using the Very Long Baseline Array (VLBA¹) operating in the 43 GHz band, and augmented at most epochs by a single antenna from the Very Large Array². Both telescopes are operated by the National Radio Astronomy Observatory (NRAO³). Auxiliary VLA interferometer observations were scheduled throughout the period of the VLBA observations, to allow absolute calibration of the EVPA of the linearly-polarized SiO emission. Both the VLBA and VLA observations and data reduction are discussed in further detail below. Optical variability data, showing the pulsation phases in relation to the scheduling of these

¹<http://vlba.aoc.nrao.edu>

²<http://vla.aoc.nrao.edu>

³The National Radio Astronomy Observatory is a facility of the National Science Foundation, operated under cooperative agreement by Associated Universities, Inc.

VLBA observations, is shown in Figure 1, reproduced here from Paper I.

2.1. VLBA Observations and Reduction

The data were recorded at each antenna in dual-circular polarization in two 4 MHz baseband spectral windows, each digitally sampled at the full Nyquist rate of 8 Mbps in 1-bit quantization. The lower spectral window was centered at a fixed topocentric frequency corresponding to the $v = 1$, $J = 1 - 0$ SiO transition, at an assumed rest frequency $\nu_0 = 43.122027$ GHz and a systemic velocity $V_{LSR} = +9$ km s⁻¹ toward TX Cam, Doppler-shifted to the center of the array and the midpoint of the observations at each epoch. No further real-time Doppler corrections were applied; these were performed in post-processing. For the majority of the VLBA epochs in Table 1, the $v = 2$, $J = 1 - 0$ transition was simultaneously observed, and centered in the second spectral window; the analysis of these data will be presented in a future paper

Each VLBA observing epoch was scheduled in a comparable local sidereal time (LST) range, as permitted by telescope operations. Three fixed schedule formats were used over the course of these observations. For epochs {A-O} a schedule of 6-hour duration was used, balanced between the target source, TX Cam (3.5 h), the primary continuum calibrator, J0359+509 (1.1 h), and secondary calibrators 3C454.3, J0609-157, and 3C286 (each 0.22 h). A single scan on 3C286 was included initially to explore an alternative absolute EVPA calibration method, as discussed further below. This was not successful however, and for epochs {P-X} the 3C386 scan was re-allocated to TX Cam (3.6 h), and the schedule re-balanced. For epochs {Z-AQ}, an 8-hour schedule format was used, but 2 hours of each run were shared with a 22 GHz project, leaving the total 43 GHz observing time, and its division between sources, unchanged.

The data were correlated at the VLBA correlator in Socorro, NM, adopting a field center position for TX Cam of ($\alpha_{J2000} = 05^h00^m51^s.186$, $\delta_{J2000} = 56^d10^m54^s.341$). The correlator accumulation interval Δt_c was constrained by output data rate limits in place at the correlator at that time. A value $\Delta t_c = 6.03$ s was used for epochs {A-G,I-K}, and reduced to $\Delta t_c = 4.98$ s for epochs {H,M-AR}. All polarization correlation products (RR,RL,LR,LL) were formed in each correlation accumulation interval from the dual-circular data acquired at each antenna. In this spectral-line polarization mode the VLBA correlator has a channel count limit of $N_{chan} = 128$. This produced auto- and cross-power spectra in each 4 MHz baseband with a nominal velocity spacing of ~ 0.2 km s⁻¹.

The measured visibility data were reduced using spectral-line polarization calibration

methods described by Kembball, Diamond, & Cotton (1995) and Kembball & Diamond (1997), as implemented in a semi-automated pipeline using a modified version of the AIPS⁴ package maintained by the NRAO. These analysis methods are optimized for the reduction of spectral-line polarization VLBI observations of the type described here; in particular they make no implicit assumption that Stokes $V = 0$. The SiO molecule is non-paramagnetic, and the mean degree of circular polarization in the SiO maser rotational transitions is small but not zero, $m_c \sim 1 - 3\%$ (Barvainis et al. 1987; Kembball & Diamond 1997). In the data reduction method employed here, all antenna-based group delay, fringe-rate, and phase calibration, including final phase self-calibration, was performed relative to a reference antenna in a reference receptor polarization. This calibration was transferred to the orthogonal receptor polarization by solving for all relevant phase and group delay offsets using continuum calibrator observations. This generalized reduction method retains positional coincidence between Stokes I and V images, while making no implicit assumption that Stokes V is identically zero (Kembball, Diamond, & Cotton 1995). Amplitude calibration was performed with the same goal of preserving the low Stokes V signature. Each circular receptor polarization was calibrated independently using the method of Reid *et al.* (1980) to fit the autocorrelation spectra in each receptor polarization to a template reference spectrum in that polarization. The template spectra in each receptor polarization were calibrated on an absolute scale using system temperature measurements reported during the observations and known point-source sensitivities and gain curves published for the VLBA antennas. A final single differential polarization gain correction was determined by cross-fitting the spectra between receptor polarization at the template scan to measure a relative scale factor. For the low integrated m_c known for SiO masers, this approximation is warranted for the integrated autocorrelation spectrum; it would not be appropriate for individual cross-power spectra, for example, as some SiO maser components can be substantially circularly polarized (Kembball & Diamond 1997). This final differential polarization gain correction adjusts for errors in the reported system temperatures and point source sensitivities, as used in the a priori absolute calibration of the template spectrum in each receptor polarization. We estimate these uncertainties very approximately as 5-10% for the VLBA at this frequency. We do not correct for atmospheric opacity at the pointing position and time of observation of the template spectrum for the data reported here. However, this has no polarization dependence, and accordingly does not affect our measurement of linear or circular polarization percentage or orientation; it only introduces a modest uncertainty in our absolute flux density scale. This uncertainty is mitigated by the fact that the template spectrum is chosen for its signal-to-noise ratio (SNR) and peak magnitude; these factors ensure that it is almost

⁴<http://www.aips.nrao.edu>

always at a sufficiently high elevation to minimize atmospheric opacity contributions.

As phase self-calibration is used, our final VLBA images of the SiO maser emission toward TX Cam retain no absolute astrometric information or alignment. In Paper I, zeroth frequency-moment total intensity images from successive epochs were initially aligned using spatial cross-correlation. This initial alignment was then refined using feature-based registration in which the deviation in proper motion paths predicted for individual maser components was minimized. For the polarization and total intensity images produced and reported in the current reduction, we adopt the alignment frame developed in Paper I as an absolute reference. Each of the zeroth-moment total intensity images produced in the current work was registered relative to its corresponding epoch in the Paper I frame using Fourier-based matched filtering. A robust, weighted-sum estimator of the filter output peak was used to measure the two-dimensional spatial offsets. This was found to out-perform an elliptical Gaussian fit to the peak, likely because it is less sensitive to small morphological differences in the total intensity images being aligned. Based on manual cross-checks of the positions of individual SiO maser components, we believe the registration of our polarization images relative to the alignment frame determined in Paper I has an accuracy of $100\mu\text{as}$ or less. Note that the images in Paper I used to produce the Stokes I movie published there were enhanced in contrast by applying the transformation \sqrt{I} and a subsequent threshold cutoff $\sqrt{I} < 0.7$. For consistency, the same transformation was applied to the total intensity images reduced here before the matched filter alignment.

The calibrators, J0359+509, 3C454.3, and J0609-157 were reduced separately using continuum polarization VLBI techniques for millimeter wavelength observations described by Kembell, Diamond, & Pauliny-Toth (1996). As the only calibrator source with sufficient parallactic angle coverage, continuum instrumental polarization leakage terms were determined from the observations of J0359+509 alone and applied to the other calibrator sources. Continuum polarization images in Stokes (I, Q, U) were then produced for each calibrator at each epoch. As noted above, the calibrators 3C454.3 and J0609-157 were only observed for a single 13-min scan at each epoch, primarily as visibility calibrators, and have limited image sensitivity and poor uv -coverage as a result. The image quality for these sources was accordingly often poor, especially for 3C454.3, which has more complex structure (Kembell, Diamond, & Pauliny-Toth 1996) than the more compact J0609-157.

2.2. VLA Observations and Reduction

The absolute EVPA of any linearly-polarized emission measured in our VLBA observations is unknown as no instrumental measurement of the absolute R-L phase difference at the

reference antenna is possible. Although the VLA similarly lacks the capability to make this measurement, it can provide absolute astronomical calibration of EVPA relative to a small subset of primary polarization calibrators given the lower spatial resolution of the array.

We have adopted the traditional approach of calibrating the EVPA of our VLBA observations by using the VLA to transfer absolute polarization calibration to these data via a sufficiently compact secondary polarization calibrator suitable for imaging with both arrays. We use the continuum source J0359+509 as this transfer calibrator. Short (1-2 h) VLA observations were accordingly requested across the time-span of our VLBA observations, and were scheduled when logistically possible on the VLA. The dates of the auxiliary VLA observation associated with our TX Cam monitoring campaign are listed in Table 2.

In these VLA observations we measured the absolute EVPA of J0359+509 relative to the primary polarization calibrator 3C138, which is the only primary polarization calibrator available in this right ascension range. Our observations were primarily scheduled in continuum mode, observing with two 50 MHz spectral windows and full polarization. Instrumental polarization calibrators were chosen separately for each VLA run, as it was not possible to schedule these observations in identical local sidereal time ranges. Each observation included J0359+509 and 3C138 however, in order to address the primary scientific goal.

Two dominant sources of systematic error affected these observations: i) their short duration, which at times limited the fidelity of the instrumental polarization calibration due to the reduced parallactic angle range; and ii) the extended structure of 3C138 at this angular resolution and observing frequency, making it a sub-optimal polarization reference in the long-baseline VLA configurations. The deficiencies in 3C138 notwithstanding, it remained our only viable primary polarization calibrator in this LST range.

The data were reduced using standard heuristics for Q-band VLA observations, as described in an appendix of the AIPS cookbook (Greisen *et al.* 2007). During data loading, an opacity correction was applied using a weighted estimate of the zenith opacity based on the surface weather, with a relative weight of 0.75, and a seasonal model, weighted by 0.25. A standard gain curve supplied for the VLA was used. Post-facto antenna-position corrections were then applied as needed. All subsequent reduction was performed for each 50 MHz spectral window independently. The data were edited interactively and the primary flux scale established for 3C138 using the model provided within the AIPS package. An initial phase calibration over a solution interval of 20 s was performed, using an a priori model for 3C138 (to mitigate source resolution) and any uv-range limits recommended for other calibrators in the schedule, but which were otherwise assumed to be point sources. An amplitude gain correction was then determined for each antenna, scan, and receptor polarization on each continuum source. This allowed the flux density of the continuum calibrators

other than 3C138 to be determined relative to the prior flux density scale established for 3C138. A joint solution for instrumental polarization was performed across all continuum calibrators, and final images in Stokes (I, Q, U) produced for each continuum source in each 50 MHz spectral window separately. An image pixel spacing of $\frac{1}{10}$ th of the expected spatial resolution in each VLA configuration was adopted, assuming that the VLA configurations have the following spatial resolutions at 43 GHz: A) 0.05"; B) 0.15"; C) 0.47"; and, D) 1.5" (Ulvestad, Perley, & Taylor 2007). For hybrid configurations, such as AB, the geometric mean of the nominal resolution in each configuration was used. The images were cleaned to the 1σ thermal noise limit predicted for each source based on the number of calibrated visibilities, time and frequency averaging, and known system equivalent flux density.

The absolute EVPA of J0359+509 was determined separately in each 50 MHz spectral window, relative to the value measured for 3C138 in that window, here assumed to have an absolute EVPA $\chi_{EVPA} = -14^\circ$ (Perley & Taylor 2003). The final absolute EVPA χ of J0359+509 was computed as the mean of the EVPA measured independently in each 50 MHz spectral window, here denoted by subscripts 1 and 2, with an estimated standard error $\epsilon_\chi = \frac{1}{\sqrt{2}}|\chi_1 - \chi_2|$. This error estimate is approximate due to the small number of independent measurements. The measured absolute EVPA for J0359+509 is listed in Table 2 and plotted in the top panel of Figure 2. A weighted cubic polynomial fit over a scrolling window five samples wide is drawn as a solid line in the upper panel. This fit was used to interpolate the absolute EVPA measured with the VLA to the dates of the VLBA observations, as listed in Table 1. We note however that the VLA data are sparsely-sampled in time, especially during a sharp rise in EVPA in late 1998. Continuum extra-galactic sources are significantly variable in linear polarization, and this interpolation scheme does not capture all source variability at the current sampling.

The EVPA measured for J0359+509 in the VLBA observations is plotted in the middle panel in this figure. This measured EVPA is not absolutely calibrated and is instead uncertain by an additive rotation equal to half the RCP-LCP phase difference at the VLBA reference antenna, which in the VLBA reduction was chosen to be Los Alamos. Error bars σ_χ were estimated approximately for the VLBA continuum polarization images from the measured off-source rms, σ_Q and σ_U , in Stokes Q and U respectively as $\sigma_\chi = \frac{1}{2(Q^2+U^2)} \sqrt{\sigma_u^2 Q^2 + \sigma_q^2 U^2} \sqrt{\frac{1}{N}}$, where N is the number of pixels over which (Q, U) were measured, and σ_Q and σ_U were corrected for noise correlation resulting from convolution with the restoring beam (of mean FWHM $\sim 300\mu\text{as}$) using the relation given by Condon (1991).

The predicted EVPA rotation for each epoch, obtained as the difference between the interpolated VLA and measured VLBA EVPA at each epoch, is plotted as a series of points in the lower panel. We expect, from instrumental considerations, that the RCP-LCP phase

difference at a VLBA antenna should be relatively stable over long periods, barring any changes in receivers or electronics. We note the bimodal distribution of points that has a vertical break coinciding with the only receiver change at the reference antenna (Los Alamos) during the period of these observations. This occurred on 30 April 1998. Accordingly, we fit a cubic polynomial to the data separately on either side of this break to derive the final EVPA rotation per epoch. This was the lowest-order polynomial to yield a reasonable fit to the data. The significant deviations in late 1998 are likely due to the systematic under-sampling of the VLA EVPA measurements during this period, as noted above. We estimate the peak-to-peak error in absolute EVPA alignment at $\sim 10^\circ - 20^\circ$ using this method.

3. Results and Discussion

The total and linearly-polarized intensity images of the $v = 1$, $J = 1 - 0$ SiO emission toward TX Cam over the pulsation phase range covered by this paper are shown in Figures 3 through 9. In these composite figures, the enhanced-contrast Stokes I image is plotted as a background contour plot, overlaid by vectors representing the linearly-polarized emission. The vectors are drawn with a length proportional to the linearly-polarized intensity and at the position angle (N through E) corresponding to the EVPA of the linearly-polarized emission. These figures are the zeroth-moment (over frequency) of the associated Stokes (I, Q, U) brightness in the parent image cubes at each epoch.

These polarization images are presented in an animated sequence in the electronic materials associated with this paper, in the form of a movie of the linear polarization morphology evolution of the $v = 1$, $J = 1 - 0$ SiO maser emission toward TX Cam over the pulsation phase range $\phi = 0.68$ to $\phi = 1.82$.

The phase range covered is the first pulsation cycle of our longer synoptic monitoring campaign. Several striking properties are evident from this time-series of figures. Over this pulsation phase range, the linear polarization EVPA is predominantly tangential to the projected total intensity SiO maser shell. In addition, for the majority of the SiO maser components, the EVPA of individual features appears to persist over their component lifetimes. Finally, the linearly-polarized intensity of the maser emission is generally brightest at the inner projected shell boundary and decreases in magnitude at larger radii.

The dominant tangential linear-polarization morphology is consistent with that reported by Kembell & Diamond (1997) at a single epoch, in the first VLBI imaging polarimetry of this SiO transition toward TX Cam. The earlier observations were undertaken on 1 Dec 1994, so precede the data in the current paper by two pulsation cycles. Desmurs et al. (2000)

confirmed the tangential linear polarization morphology toward TX Cam in observations in April 1996. Taken together with the current data, this suggests that this morphology may be an inter-cycle property of the SiO maser emission toward this star. It is not yet clear however, whether this is a generic property of SiO linear polarization in this transition toward late-type evolved stars in general. Desmurs et al. (2000) report a similar tangential morphology in the SiO maser emission toward IRC+10011. However, for a sample of Mira variables monitored in $v = 1, 2$, $J = 1 - 0$ SiO maser emission in a full-polarization VLBI imaging study, and reported in a series of papers by Cotton, Perrin, & Lopez (2008, and references therein), the results are more mixed. Early images suggested no pervasive linear polarization pattern (Cotton *et al.* 2004); however, later, a bimodal EVPA distribution (in the sense of being either parallel or perpendicular to the projected shell) was reported for U Ori and o Cet (Cotton *et al.* 2006). However, not all sources for which images are shown by Cotton, Perrin, & Lopez (2008) show tangential linear polarization structure. Further observations of larger samples are needed to resolve this important question.

There are several possible theoretical explanations for tangential linear polarization structure in SiO maser emission, as we see in the data presented here. However, these interpretations are conditional on the theoretical assumptions made concerning the underlying maser emission; we focus here only on the observational implications of these theoretical issues in what follows.

Silicon monoxide is a non-paramagnetic molecule and the rotational transition considered here is in the small-splitting Zeeman regime. Following Elitzur (1996), the ratio x_B of the Zeeman splitting to the Doppler linewidth Δv_D is (Kemball & Diamond 1997):

$$x_B = 8.2 \times 10^{-4} \left(\frac{B}{\text{G}} \right) \left(\frac{\Delta v_D}{\text{km.s}^{-1}} \right)^{-1} \quad (1)$$

For the case of $x_B \ll 1$, as equation 1 indicates is applicable to SiO, competing models for the transport of polarized maser emission have been presented (Elitzur 1996; Watson 2002, and references therein). Both series of papers extend the parameter space and generalize the original foundational work of Goldreich, Keeley, & Kwan (1973). There also remains uncertainty in the literature as to whether SiO masers are pumped by collisional (Elitzur 1980) or radiative mechanisms (Bujarrabal & Nguyen-Q-Rieu 1981). Finally, an additional consideration is the degree to which m -anisotropic pumping of the magnetic substates dominates. We neglect for the purposes of this discussion the role of magnetic or velocity gradients in the masing regions, and any considerations that apply specifically to transitions with spins higher than $J = 1 - 0$.

At the outset we need to determine in which theoretical regime of maser polarization

propagation our observational data reside. Specifically, there are several key parameters that determine this theoretical interpretive framework. These include the relative magnitude of the stimulated emission rate, R , the cumulative collisional and radiative decay rate, Γ , and the Zeeman rate, $g\Omega$ (Goldreich, Keeley, & Kwan 1973; Watson 2002).

To estimate R , we adopt equation 1 of Plambeck, Wright, & Rao (2003) to derive the stimulated emission rate of the $v = 1$, $J = 1 - 0$ SiO transition as:

$$R = 23 \left(\frac{T_B}{2 \times 10^{10} \text{ K}} \right) \left(\frac{d\Omega}{10^{-2} \text{ sr}} \right) \text{ s}^{-1} \quad (2)$$

where T_B is the maser brightness temperature and $d\Omega$ is the estimated maser beaming angle. The relative magnitude of R and Γ defines the degree of maser saturation, with saturation increasing for increasing $\frac{R}{\Gamma}$. The vibrational radiative transitions $v \rightarrow (v - 1)$ for low- J rotation levels have radiative decay rates $\Gamma \sim 5v \text{ s}^{-1}$ (Kwan & Scoville 1974; Elitzur 1992). These radiative decay rates dominate over SiO-H₂ or SiO-H collisional de-excitation. From the collisional rate equations in Elitzur (1980), we calculate $\Gamma < 1 \text{ s}^{-1}$ for collisions, adopting a representative temperature $T=1300 \text{ K}$ and atomic hydrogen density $n_H = 5 \times 10^{10} \text{ cm}^{-3}$ in the SiO maser region, as inferred from Reid & Menten (1997). The Zeeman rate for SiO is given by Nedoluha & Watson (1990); Plambeck, Wright, & Rao (2003) as:

$$\frac{g\Omega}{2\pi} \sim 200 \left(\frac{B}{G} \right) \text{ s}^{-1} \quad (3)$$

In the limiting regime $g\Omega \gg R \gg \Gamma$, and assuming m -isotropic pumping, the Goldreich, Keeley, & Kwan (1973) solutions for the linear polarization are applicable. In this case the fractional linear polarization depends on the angle between the line of sight and the magnetic field, and takes the form $q(\theta) = \frac{Q}{I} = \frac{2-3\sin^2\theta}{3\sin^2\theta}$ for $\theta \geq \theta_B$, and $q(\theta) = 1$ for $\theta \leq \theta_B$, where $\theta_B \approx 35^\circ$ (Goldreich, Keeley, & Kwan 1973; Elitzur 1992). At a break angle, $\theta_F \approx 55^\circ$, defined as the point where $\sin^2\theta_F = \frac{2}{3}$, and Stokes Q changes sign, the observed EVPA on the plane of the sky switches from parallel to the projected magnetic field ($\theta < \theta_F$) to perpendicular to the projected magnetic field ($\theta > \theta_F$) (Goldreich, Keeley, & Kwan 1973; Elitzur 1992). We note that this change of EVPA over 90° has been detected observationally by Vlemmings & Diamond (2006) for a water maser component in the source W43A.

The degree of saturation $\frac{R}{\Gamma}$ required to achieve the the limiting magnitude of fractional linear polarization differs however between the two theoretical models of maser polarization propagation (Nedoluha & Watson 1990; Elitzur 1996). A saturation of $\frac{R}{\Gamma} \approx 30$ is required to achieve 70% linear polarization in the models summarized by Watson & Wyld (2001). In

the model of Elitzur (1996), however, the full polarization solution is realized well before saturation.

In addition, the observational interpretation of linearly-polarized SiO maser emission is further influenced by whether the maser inversion is assumed to be due to collisional or radiative pumping. If the pumping is assumed to be radiative, then the effects of m -anisotropic pumping of the magnetic sublevels m of the rotational transitions needs to be considered (Bujarrabal & Nguyen-Q-Rieu 1981) along with related radiative effects (Ramos, Degl’Innocenti, & Bueno 2005). In the case of stellar SiO masers, there is an inherent anisotropy in the angular distribution of the photons from the central star incident on the masing region, and, in this model, m -anisotropic pumping can produce large linear polarization magnitudes, oriented tangentially to the incident radial stellar photons (Western & Watson 1983; Desmurs et al. 2000). For m -anisotropic pumping, the observed EVPA is still likely to be either parallel or perpendicular to the projected magnetic field on the plane of the sky, if the conditions $g\Omega > R$ and $g\Omega > \Gamma$ hold, even weakly (Watson 2002), however the shape of the function $q(\theta)$ and the break angle θ_F are likely to differ from the standard Zeeman case above. If the magnetic field is sufficiently weak so that $g\Omega \approx R$ holds, then the EVPA need no longer be strictly parallel or perpendicular to the magnetic field in this model (Watson 2002). Given the degree of order we observe in the linear polarization morphology, the data suggest that $g\Omega \neq R$ in the current study.

Both theoretical models of maser polarization predict circular polarization that is broadly proportional to the magnetic field strength (Watson & Wyld 2001; Elitzur 1996), but with differences in predicted line-shape and dependence on saturation as well as the angle θ between the magnetic field and the line of sight. Given x_B for SiO masers, circular polarization at the several percent level predicts Gauss-level magnetic fields (Barvainis et al. 1987; Kemball & Diamond 1997). In the models summarized by Watson (2002), circular polarization can also arise from non-Zeeman effects caused by a difference between the optical axes along the maser propagation path and the direction of linear polarization. Circular polarization can be produced in this model when $R \approx g\Omega$ (Nedoluha & Watson 1990) or by turbulent rotation of the magnetic field along the line of sight in the regime $g\Omega \gg \{R, \Gamma\}$ (Wiebe & Watson 1998).

To constrain the theoretical regime in which our current data reside, it is first useful to estimate the relative magnitude of $g\Omega$, R , and Γ . There are two main sources of uncertainty in this estimation, namely the strength of the magnetic field, B , and the unknown maser beaming angle $d\Omega$ used to calculate the stimulated emission rate in equation 2 (equivalently, the degree of saturation). We make an initial estimate of B by comparing energy densities. A magnetic field B implies a magnetic energy density:

$$\frac{B^2}{2\mu_0} \sim 4 \times 10^{-3} \left(\frac{B}{\text{G}}\right)^2 \text{ J.m}^{-3} \quad (4)$$

For our adopted $n_H = 5 \times 10^{10} \text{ cm}^{-3}$ and $T = 1300 \text{ K}$, the thermal energy density is $\frac{3}{2}n_H kT \sim 1.3 \times 10^{-3} \text{ J.m}^{-3}$, and the bulk kinetic energy density is $\frac{1}{2}\rho v^2 \sim 2.0 \times 10^{-3} \text{ J.m}^{-3}$, where ρ is density and we adopt a bulk motion $v = 7 \text{ km s}^{-1}$ from Paper I. Equating these energy densities suggests a zeroth-order magnetic field estimate in the range $\sim 580 - 720 \text{ mG}$. For $B \sim 0.6 \text{ G}$, equation 3 predicts $\frac{g\Omega}{2\pi} \approx 120 \text{ s}^{-1}$. Tangential shock compression driven by stellar pulsation could increase the magnetic field strength by an order of magnitude (Soker 2002; Hartquist & Dyson 1997). Adopting $R \sim 23 \text{ s}^{-1}$, $\Gamma \sim 5 \text{ s}^{-1}$, and $g\Omega \geq 10^{3-4}$, would place us in the regime: $g\Omega \gg R \gg \Gamma$ or $g\Omega > R \gg \Gamma$. In this regime, and absent significant Faraday rotation, the standard Zeeman interpretation of the parallel or perpendicular orientation of the EVPA relative to the projected magnetic field would apply, and the linearly-polarized morphology could either be tracing a globally-organized stellar magnetic field, or a sparse strong field that is only dynamically significant on local scales. There are arguments against a globally organized stellar magnetic field in isolated (non-binary) TP-AGB stars, primarily the likely low rotation velocity at this point in their evolutionary path in the H-R diagram, and the difficulties of sustaining a regular $\alpha\omega$ dynamo in stars with such an extended mantle, amongst other considerations (Soker 2006). However, as noted above, there are several strands of observational evidence supporting surface magnetic fields of order 10^{2-3} G in Mira variables (Vlemmings, van Langevelde, & Diamond 2005) and the central stars of PNe (Jordan, Werner, & O’Toole 2005) respectively, as well as magnetic jet collimation in post-AGB transition objects (Vlemmings, Diamond, & Imai 2006).

A sparse field in an AGB extended atmosphere could arise from an $\alpha^2\omega$ convective dynamo, as noted above, and might include local loops rising above the photosphere, other flaring events, and magnetic cool spots (Soker & Clayton 1999; Soker & Kastner 2003). These localized fields are also expected to be shock-compressed tangentially due to the outwardly-propagating shock waves from the pulsating central star, introducing a preferred geometry for field enhancement. This is a complex three-dimensional picture, but it is also important to remember that SiO masers sample only those regions of the NCSE that lie relatively close to the orthogonal plane to the line of sight. This constraint arises from the observed tangential amplification of the total intensity emission.

If however, the masers are pumped radiatively and the radiative pumping is m -anisotropic, then the tangential linear polarization morphology could originate from that mechanism (Western & Watson 1984), even in the non-magnetic case $g\Omega \sim 0$ (Ramos, Degl’Innocenti, & Bueno 2005). For the magnetic case, $g\Omega > 0$, the Hanle effect can, in certain cases, produce an

EVPA rotation exceeding 45 deg relative to the tangential direction (Ramos, Degl’Innocenti, & Bueno 2005). In the case of m -anisotropic pumping in general, we would also expect to measure a functional shape for $q(\theta)$, and associated break angle θ_F , that differs from the standard Zeeman form noted above (Western & Watson 1984), and a higher degree of linear polarization magnitude (Watson 2002).

In Figure 10 we examine the variation of mean fractional linear polarization magnitude $\overline{m}_l(\phi)$ against pulsation phase. This value was computed at each epoch from the sum of Stokes I and $P = \sqrt{Q^2 + U^2}$, using a pixel mask defined as the set of all pixels with a total intensity exceeding three times the Stokes I image rms, and corrected for statistical bias in P . The value of $\overline{m}_l(\phi)$ has a minimum near $\phi \sim 1$ and a maximum near $\phi \sim 1.5$. It has higher values when the inner edge of the shell is well-defined and dominates the overall total intensity morphology. Unfortunately this result can be interpreted either as evidence for linear polarization driven primarily by magnetic field enhancement through shock compression, or is supportive of m -anisotropic pumping as the dominant origin of linear polarization: both are expected to be stronger in the inner shell boundary. We note that the mean fractional linear polarization is broadly inversely correlated with the shell width.

We identify several key uncertainties that need to be further constrained by observations before the remaining theoretical polarization transport uncertainties can be resolved, and that are amenable to observational tests: i) the statistical incidence of tangential linear polarization morphology in Mira variables as a class; ii) independent measurement of the exact degree of saturation of stellar SiO masers; and iii) detailed measurements of the functional form of $q(\theta)$ in maser regions where this is possible. We plan to address these issues in future papers. As yet, there is insufficient observational data to distinguish the relative influence of m -anisotropic pumping on the magnitude or orientation of the linearly-polarized SiO emission

The linear polarization maps we present here have significant fine-scale, locally-ordered, polarization structure, as noted in the first SiO polarization observations of TX Cam by Kemball & Diamond (1997). Recently, in their sample of O-rich AGB stars, Cotton, Perrin, & Lopez (2008) have cited locally-ordered polarization morphologies along jet-like features pointing radially toward the central star. Due to the persistence of the SiO linear polarization properties over a sufficient fraction of the component lifetime in the polarization movie presented here, we are able to explore the time evolution of the polarization morphology for individual maser components. In this paper we undertake a preliminary analysis confined to two isolated components selected subject to the criteria that they: i) follow continuous trajectories across a sufficient range of epochs; ii) are located at a larger projected separation from the

inner shell boundary, so as to minimize the possible impact of strong anisotropic pumping effects; and, iii) have compact structure and high SNR.

In Figure 11 we show this analysis for a prominent infalling component at the center north of the projected shell, that is visible over epochs {S-AH}. In Figure 11, the linear polarization structure of this northern component is shown at the twelve epochs {T,U,V,W,X,Z,AA,AB,AC,AD,AE,AG} spaced along the trajectory over time, using the same composite representation of linearly-polarized emission as used in Figures 3 to 9, but with a more finely-sampled total intensity contour scale, described in further detail in the figure caption. The outermost epochs {S,AH} of the component trajectory are omitted due to the low SNR when the component appears and disappears. In common with Figures 3 to 9, each panel in Figure 11 is a zeroth-moment image over frequency; the pronounced component elongation visible in these zeroth-moment component images at several epochs along the trajectory is most readily explained in terms of a velocity gradient along the elongation major axis. These velocity gradients are most directly assumed to arise from linear acceleration along a three-dimensional component trajectory inclined to the line of sight to the observer. The weighted-mean component positions, with associated error bars, are plotted in Figure 12 for each epoch along the trajectory. At each component position in this figure, a bold vector of uniform length (over epoch) is drawn at the orientation of the integrated component EVPA. A least-squares fit to the component positions, incorporating x- and y-errors, was performed using software described by Weiner *et al.* (2006). The fitted mean projected trajectory is extrapolated in Figure 14 across the full diameter of the SiO maser shell at epoch {Z}, here chosen as an epoch near the mid-point of the northern component trajectory shown in Figure 12. Figure 14 shows that the projected component trajectory is non-radial with respect to the likely stellar position relative to the SiO shell distribution; this qualitative assertion remains valid within the statistical errors of the projected linear fit parameters. If dynamically-significant gas pressure gradients are not present, then purely gravitational infall would be radial toward the central star. We note that this component has an EVPA oriented predominantly orthogonal to the projected proper motion vector. As noted above, the location of this component is at a significantly larger radius than the inner shell boundary, and therefore minimizes the possibility of strong anisotropic pumping effects. Over parts of the earlier epoch range {C-N}, a component is visible approximately 3.25 mas to the east of the northern component considered here. This north-eastern component is at a significantly lower SNR, and is not clearly detected in linear polarization at epochs {G-I,M-N} as a result. Given the proximity to the northern component, however, we plot the counterpart of Figure 12 for this component as Figure 13. This shows the north-eastern component moving outward over these epochs with an EVPA again predominantly orthogonal to the projected proper motion vector.

A second isolated component is visible over epochs {AA-AL} to the east of the mid-latitude of the projected shell, and we plot the counterparts of Figures 11-12 for this eastern component as Figures 15-16. This component is infalling over this epoch range and the EVPA is primarily either parallel or perpendicular to the projected proper motion vector.

This preliminary polarization proper motion analysis for the initial components considered here, which were chosen for their location in the outer shell where radiative anisotropic pumping effects are less likely to predominate, show two key properties: i) the inferred magnetic field orientation is likely to be parallel to the proper motion vector, as the EVPA orientation is either parallel or perpendicular to this proper motion; and ii) the motion is sometimes non-radial relative to the central star, in contrast to what is expected for ballistic motion in the stellar gravitational field. These properties are consistent with component motion along magnetic field lines in the extended atmosphere. An alternative explanation is that a local magnetic field is being dragged and elongated by the gas motion, and the component motion is not governed dynamically by the magnetic field. This explanation is not excluded however, but we believe it is not favored by the preponderance of the current observational evidence. This issue is also discussed in connection with jet-like feature extensions in the SiO images obtained by (Cotton, Perrin, & Lopez 2008).

We also observe several 90-degree EVPA reversal at the inner-shell boundary, as noted in the first TX Cam polarization imaging (Kemball & Diamond 1997). These features are particularly prominent in the south-west edge of the shell, from epochs {AJ-AR}. These EVPA reversals can be explained either as transitions across the break angle in the Goldreich, Keeley, & Kwan (1973) solutions or, in the case of m -anisotropic pumping, a transition in the degree of anisotropy (Ramos, Degl’Innocenti, & Bueno 2005). These issues will be considered in more detail in a future analysis.

4. Conclusions

We have presented a finely-sampled time series of 42 images of the linearly-polarized $v = 1$, $J = 1 - 0$ SiO maser emission toward the Mira variable, TX Cam over a pulsation phase range $\phi = 0.68$ to $\phi = 1.82$. These data augment a total intensity animated sequence previously published for this pulsation phase range by Diamond & Kemball (2003). From our initial analysis we conclude:

1. The predominant linear polarization morphology is one in which the EVPA of the linearly-polarized SiO emission is predominantly tangential to the projected shell of SiO maser emission in total intensity. This morphology is observed for all epochs

presented here.

2. The linear polarization EVPA of individual SiO maser components is relatively stable over their component lifetimes for many individual components visible in the images.
3. The magnitude of the linear polarization appears brighter at the inner region of the shell boundary, and decreases for larger radii.
4. An analysis is presented that argues that we are in the theoretical regime $g\Omega \gg R \gg \Gamma$ or $g\Omega > R \gg \Gamma$ for maser polarization propagation. There is, as yet, insufficient observational data to distinguish the relative influence of m -anisotropic pumping on the magnitude or orientation of the linearly-polarized SiO $v = 1, J = 1 - 0$ emission.
5. An initial polarization proper motion study is presented for two outer maser components that provides some supporting evidence to the argument that magnetic fields are dynamically significant in the extended atmospheres of late-type, evolved stars.

This material is based upon work supported by the National Science Foundation under Grant No. AST-0507473. Any opinions, findings, and conclusions or recommendations expressed in this material are those of the authors and do not necessarily reflect the views of the National Science Foundation. We acknowledge with thanks data from the AAVSO International Database based on observations submitted to the AAVSO by variable star observers worldwide. We thank Dr. W. Watson for reading a draft of the manuscript and for helpful comments from an anonymous referee that improved the paper.

Facilities: VLBA

REFERENCES

- Alvarez, R., Jorissen, A., Plez, B., Gillet, D., & Fokin, A. 2000, *A&A*, 362, 655
- Barvainis, R., McIntosh, G., & Predmore, C.R. 1987, *Nature*, 329, 613
- Bertshinger, E. & Chevalier, R.A. 1985, *ApJ*, 299, 167
- Bessell, M.S., Scholz, M., & Wood, P.R. 1996, *A&A*, 307, 481
- Blackman, E.G., Frank, A., Markiel, J.A., Thomas, J.H., & Van Horn, H.M. 2001, *Nature*, 409, 485

- Condon, J.J. 1991, PASP, 109, 166
- Bowen, G.H. 1988, ApJ, 329, 299
- Bujarrabal, V. & Nguyen-Q-Rieu 1981, A&A, 102, 65
- Cotton, W.D., Mennesson, Diamond, P.J., Perrin, G., Coudé du Foresto, V., Chagnon, G., van Langevelde, H.J., Ridgway, S., Waters, R., Vlemmings, W., Morel, S., Traub, W., Carleton, N., & Lacasse, M. 2004, A&A, 414, 275
- Cotton, W.D., Vlemmings, W., Menneson, B., Perrin, G., Coudé du Foresto, V., Chagnon, G., Diamond, P.J., van Langevelde, H.J., Bakker, E., Ridgway, S., McAllister, H., Traub, W., & Ragland, S. 2006, A&A, 456, 350
- Cotton, W.D., Perrin, G., & Lopez, B. 2008, A&A, 477, 853
- Desmurs, J.F., Bujarrabal, V., Colomer, F., & Alcolea, J. 2000, A&A, 360, 189
- Diamond, P.J., Kemball, A.J., Junor, W., Zensus, A., Benson, J., & Dhawan, V. 1994, ApJ, 430, L61
- Diamond, P.J. & Kemball, A.J. 599, 1372
- Dorch, S.B.F 2004, A&A, 423, 1101
- Elitzur, M. 1980, ApJ, 240, 553
- Elitzur, M. 1992, *Astronomical Masers* (Dordrecht: Kluwer)
- Elitzur, M. 1996, ApJ, 457, 415.
- Freytag, B., Steffen, M., & Dorch, B. 2002, *Astron.Nachr.*, 323, 213
- García-Segura, G., Langer, N., Różyczka, M., & Franco, J. 1999, ApJ, 517, 767
- Gray, M.D., Humphreys, E.M.L., & Yates, J.A. 1999, MNRAS, 304, 906
- Greisen, E. 2007, *AIPS Cookbook*, (Charlottesville:NRAO), <http://www.aips.nrao.edu/cook.html>
- Habing, H.J. 1996, ARA&A, 7, 97
- Herpin, F., Baudry, A., Thum, C., Morris, D., & Wiesemeyer, H. 2006, A&A, 450, 667
- Hinkle, K.H., Hall, D.N.B., & Ridgway, S.T. 1982, ApJ, 252, 697

- Hinkle, K.H., Lebzelter, T., & Scharlach, W.W.G 1997, *AJ*, 114, 2686
- Humphreys, E.M.L., Gray, M.D., Yates, J.A., Field, D., Bowen, G.H., & Diamond, P.J. 2002, *ã*, 386, 256
- Goldreich, P., Keeley, D.A., & Kwan, J.Y. 1973, *ApJ*, 179, 111
- Hartquist, T.W. & Dyson, J.E. 1997, *A&A*, 319, 589
- Jordan, S., Werner, K., & O’Toole, S.J. 2005, *A&A*, 432, 273
- Kemball, A.J., Diamond, P.J., & Cotton, W.D. 1995, *A&AS*, 110, 383.
- Kemball, A.J., Diamond, P.J. and Pauliny-Toth, I.I.K. 1996, *ApJ*, 464, L55.
- Kemball, A.J., & Diamond, P.J. 1997, *ApJ*, 481, L111
- Kholopov, P.N., Samus, N.N., Frolov, M.S., Goranskij, V.P., Gorynya, N.A., Kireeva, N.N., Kukarkina, N.P., Kurochin, N.E., Medvedeva, G.I., Perova, N.B., & Shugarov, S.Yu. 1985, *General Catalogue of Variable Stars* (Moscow Publishing House: Moscow)
- Kwan, J., & Scoville, N. 1974, *ApJ*, 194, L97
- Meixner, M., Kastner, J., Balick, B., & Soker, N. (editors) 2004, *ASP Conf. Ser. 313, Asymmetrical Planetary Nebular III: Winds, Structure and the Thunderbird* (San Francisco: ASP)
- Nedoluha, G.E. & Watson, W.D. 1990, *ApJ*, 354, 660
- Nordhaus, J., Blackman, E.G., & Frank, A. 2007, *MNRAS*, 376, 599
- Olivier, E.A., Whitelock, P., & Marang, F. 2001, *MNRAS*, 326, 490
- VLA Calibrator Manual (Socorro, NM: NRAO), <http://www.vla.nrao.edu/astro/calib/manual>
- Plambeck, R.L., Wright, M.C.H., & Rao, R. 2003, *ApJ*, 594, 911
- Porter, D., Anderson, S., & Woodward, P. 1997, *LCSE report* (U. Minnesota), <http://pinot.lcsr.umn.edu/research/RedGiant>
- Ramos, A.A., Degl’Innocenti, E.L., & Bueno, J.T. 2005, *ApJ*, 625, 985
- Reid, M.J., Haschick, A.D., Burke, B.F., Moran, J.M., Johnston, K.J., & Swenson, G.W. 1980, *ApJ*, 239, 89

- Reid, M.J., & Menten, K.M. 1997, *ApJ*, 476, 327
- Soker, N. & Clayton, G.C. 1999, *MNRAS*, 307, 993
- Soker, N. & Zoabi, E. 2002, *MNRAS*, 329, 204
- Soker, N. 2002, *MNRAS*, 336, 826
- Soker, N. & Kastner, J.H. 2003, *ApJ*, 592, 498
- Soker, N. 2006, *PASP*, 118, 260
- Ulvestad, J.S., Perley, R.A., & Taylor, G.B. (editors) 2007, *VLA Observational Status Summary* (Socorro, NM:NRAO)
- Vlemmings, W.H.T., van Langevelde, H.J., & Diamond, P.J. 2005, *A&A*, 434, 1029
- Vlemmings, W.H.T., Diamond, P.J., & Imai, H. 2006, *Nature*, 440, 58
- Vlemmings, W.H.T. & Diamond, P.J. 2006, *ApJ*, 648, L59
- Watson, W.D. & Wyld, H.W. 2001, 558, L55
- Watson, W.D. 2002, in *IAU. Symp. 206, Cosmic Masers: from Protostars to Blackholes*, ed. V. Migenes & M.J. Reid (San Francisco:ASP), 464
- Weiner, B.J., Willmer, C.N.A., Faber, S.M., Harker, J., Kassin, S.A., Phillips, A.C., Melbourne, J., Metevier, A.J., Vogt, N.P., & Koo, D.C. 2006, *ApJ*, 653, 1049
- Western, L.R. & Watson, W.D. 1983, *ApJ*, 275, 195
- Western, L.R. & Watson, W.D. 1984, *ApJ*, 285, 158
- Wiebe, D.S. & Watson, W.D. 1998, *ApJ*, 503, L71
- Yi, J., Booth, R.S., Conway, J.E., & Diamond, P.J. 2005, *A&A*, 432, 531.

Table 1. Observing dates and epochs

Epoch code	Observing date	Optical phase ^a (ϕ)
BD46A	1997 May 24	0.68 ± 0.01
BD46B	1997 June 7	0.70 ± 0.01
BD46C	1997 June 22	0.73 ± 0.01
BD46D	1997 July 6	0.75 ± 0.01
BD46E	1997 July 19	0.78 ± 0.01
BD46F	1997 August 2	0.80 ± 0.01
BD46G	1997 August 16	0.83 ± 0.01
BD46H	1997 August 28	0.85 ± 0.01
BD46I	1997 September 12	0.87 ± 0.01
BD46J	1997 September 26	0.90 ± 0.01
BD46K	1997 October 9	0.92 ± 0.01
BD46L ^b	1997 October 25	0.95 ± 0.01
BD46M	1997 November 8	0.98 ± 0.01
BD46N	1997 November 21	0.00 ± 0.01
BD46O	1997 December 5	1.03 ± 0.01
BD46P	1997 December 17	1.05 ± 0.01
BD46Q	1997 December 30	1.07 ± 0.01
BD46R	1998 January 13	1.10 ± 0.01
BD46S	1998 January 25	1.12 ± 0.01
BD46T	1998 February 5	1.14 ± 0.01
BD46U	1998 February 22	1.17 ± 0.01
BD46V	1998 March 5	1.19 ± 0.01
... ^c	1998 March 21	1.22 ± 0.01
BD46W	1998 April 07	1.25 ± 0.01
BD46X	1998 April 19	1.27 ± 0.01
BD46Z	1998 May 10	1.30 ± 0.01
BD46AA	1998 May 22	1.33 ± 0.01
BD46AB	1998 June 6	1.35 ± 0.01
BD46AC	1998 June 18	1.37 ± 0.01

Table 1—Continued

Epoch code	Observing date	Optical phase ^a (ϕ)
BD46AD	1998 July 3	1.40 ± 0.01
BD46AE	1998 July 23	1.44 ± 0.01
BD46AF	1998 August 9	1.47 ± 0.01
BD46AG	1998 August 23	1.49 ± 0.01
BD46AH	1998 September 9	1.52 ± 0.01
BD46AI	1998 September 25	1.55 ± 0.01
BD46AJ	1998 October 14	1.59 ± 0.01
BD46AK	1998 October 29	1.61 ± 0.01
BD46AL	1998 November 17	1.65 ± 0.01
BD46AM	1998 December 6	1.68 ± 0.01
BD46AN	1998 December 23	1.71 ± 0.01
BD46AO	1999 January 5	1.74 ± 0.01
BD46AP	1999 January 23	1.77 ± 0.01
BD46AQ	1999 February 6	1.79 ± 0.01
BD46AR	1999 February 19	1.82 ± 0.01

^aThe optical phase is computed using the optical maximum at MJD = 50773 cited by Gray, Humphreys, & Yates (1999), and assuming their quoted uncertainty $\Delta\phi \sim 0.01$. A mean period of 557.4 days is adopted (Kholopov et al. 1985).

^bFailed epoch, that could not be successfully reduced in full.

^cThis epoch was not scheduled.

Table 2. VLA observations of J0359+509

Epoch ^d	Source	Date	Start (IAT)	End (IAT)	χ (deg) ^a	ϵ_χ (deg) ^b	Config. ^c
A	J0359+509	1997 May 24	17:08:39	20:01:20	124.8	5.5	B
C	J0359+509	1997 Jun 23	17:37:39	19:00:20	112.1	3.6	CB
E	J0359+509	1997 Jul 24	12:35:00	14:01:49	130.2	2.6	C
G	J0359+509	1997 Aug 16	13:02:20	14:31:09	143.1	2.4	C
J	J0359+509	1997 Sep 30	10:38:20	11:34:10	157.1	0.6	CD
K ^e	J0359+509	1997 Oct 13	07:48:49	09:03:19	161.8	3.1	CD
L	J0359+509	1997 Oct 31	07:04:50	08:01:59	144.0	0.8	D
T	J0359+509	1998 Feb 08	00:02:00	00:59:29	111.6	1.7	AD
W ^f	J0359+509	1998 Apr 06	22:42:40	00:40:59	-	-	A
AA	J0359+509	1998 May 28	16:54:00	18:17:00	128.5	8.4	A
AB	J0359+509	1998 Jun 08	17:36:19	19:33:30	162.0	24.0	AB
AE	J0359+509	1998 Jul 17	15:31:39	17:30:00	144.4	3.2	B
AF	J0359+509	1998 Aug 15	15:37:10	17:05:50	149.3	2.5	B
AI	J0359+509	1998 Sep 24	11:01:10	12:52:49	150.0	1.2	B
AJ	J0359+509	1998 Oct 20	10:15:30	11:46:20	7.8	18.2	B
AL	J0359+509	1998 Nov 15	09:06:10	11:03:49	24.5	8.6	BC
AN	J0359+509	1998 Dec 22	07:38:59	09:38:19	75.6	1.5	C
AP	J0359+509	1999 Jan 22	00:11:00	03:07:09	60.1	3.7	C
AQ	J0359+509	1999 Feb 07	03:03:19	04:33:50	73.8	4.7	CD
AR	J0359+509	1999 Mar 09	01:07:39	03:05:50	75.2	6.5	D

^aAbsolute electric vector position angle (EVPA) of the linearly-polarized emission from J0359+509, relative to an assumed EVPA for 3C138 at 43 GHz of $\chi_{3C138} = -14$ deg (Perley & Taylor 2003).

^bEstimated standard error in χ , derived from independent analyses of each 50 MHz VLA continuum spectral window, as $\frac{1}{\sqrt{2}}|\chi_1 - \chi_2|$.

^cVLA configuration code.

^dNearest BD46 epoch in Table 1.

^eEVPA measurement from VLBA project BK50 (Mittra *et al.*, in preparation).

^fData were not reducible at this VLA epoch.

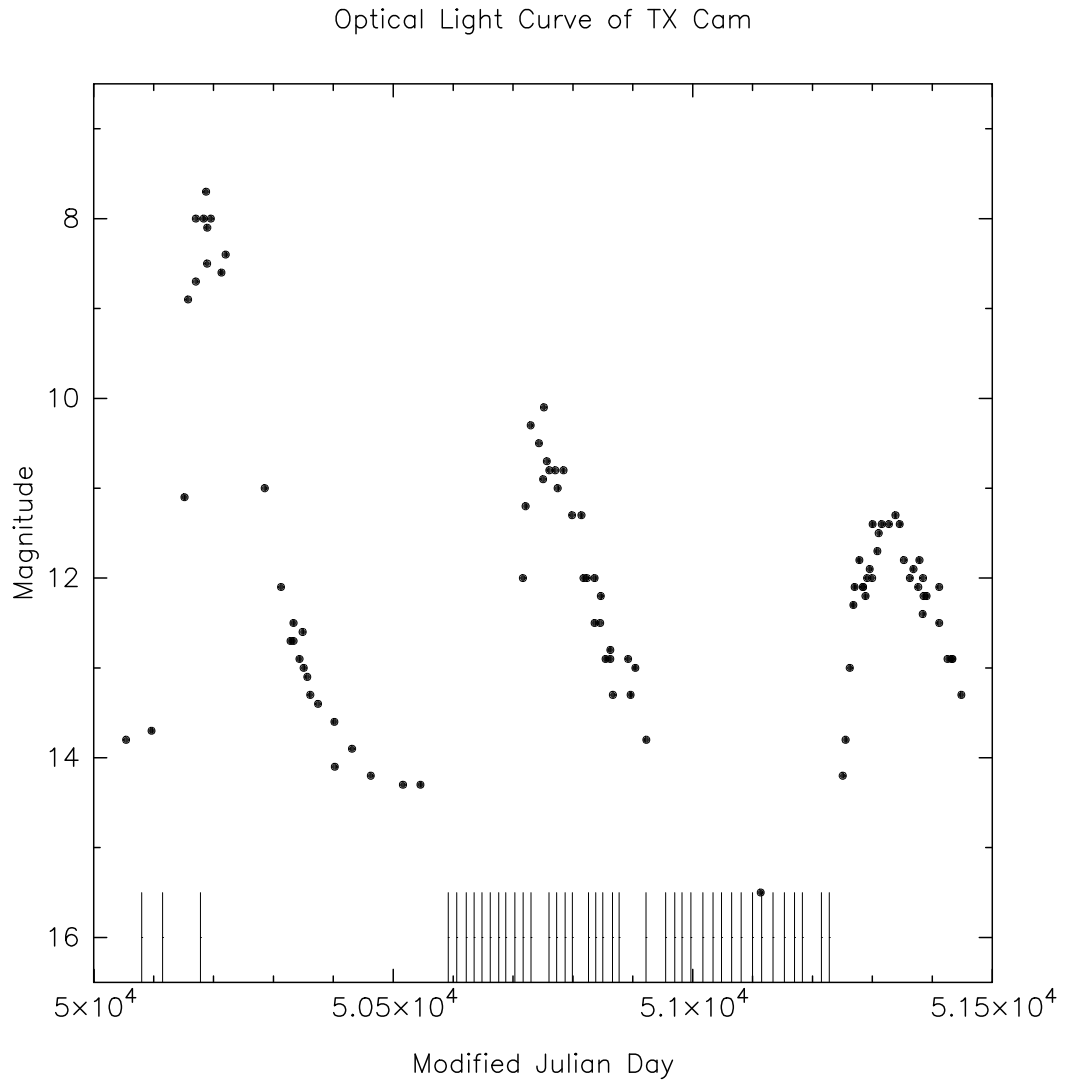


Fig. 1.— The optical light curve of TX Cam as provided by the AAVSO. The markers at the base of the figure indicate the dates of the VLBA 43 GHz observations. Reproduced from Figure 1 of Paper I.

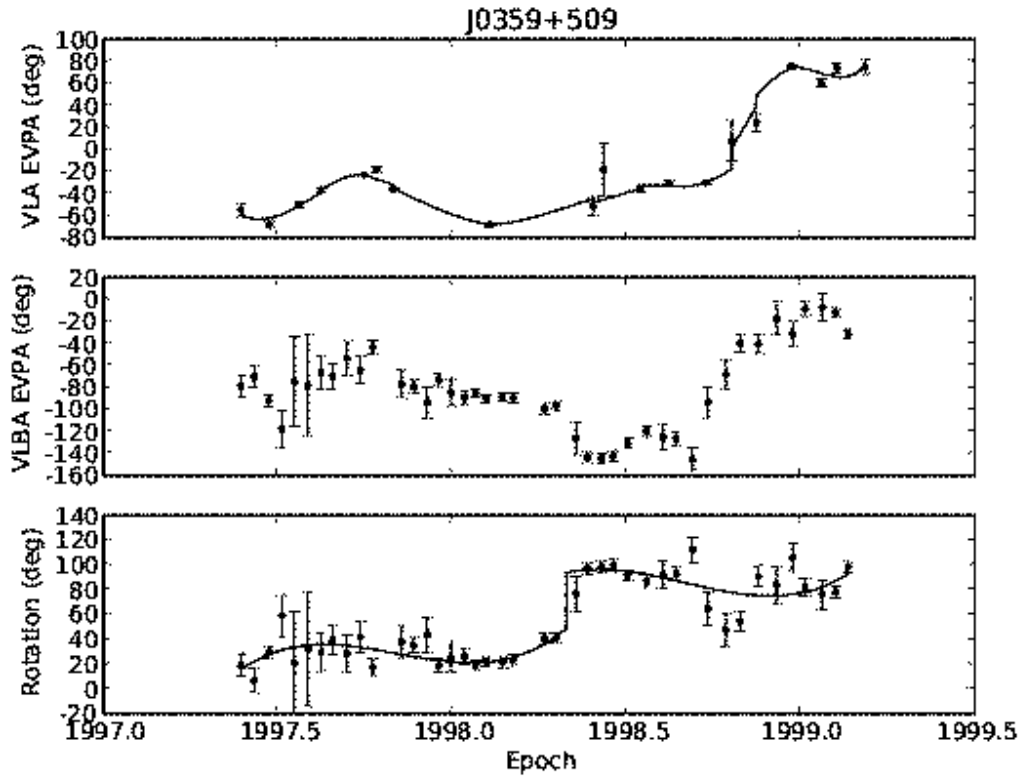


Fig. 2.— The measured VLA absolute EVPA of J0359+509 (*upper panel*), the VLBA EVPA (*middle panel*), and the difference (*lower panel*), equivalent to the EVPA rotation needed to calibrate the absolute EVPA of the VLBA polarization images.

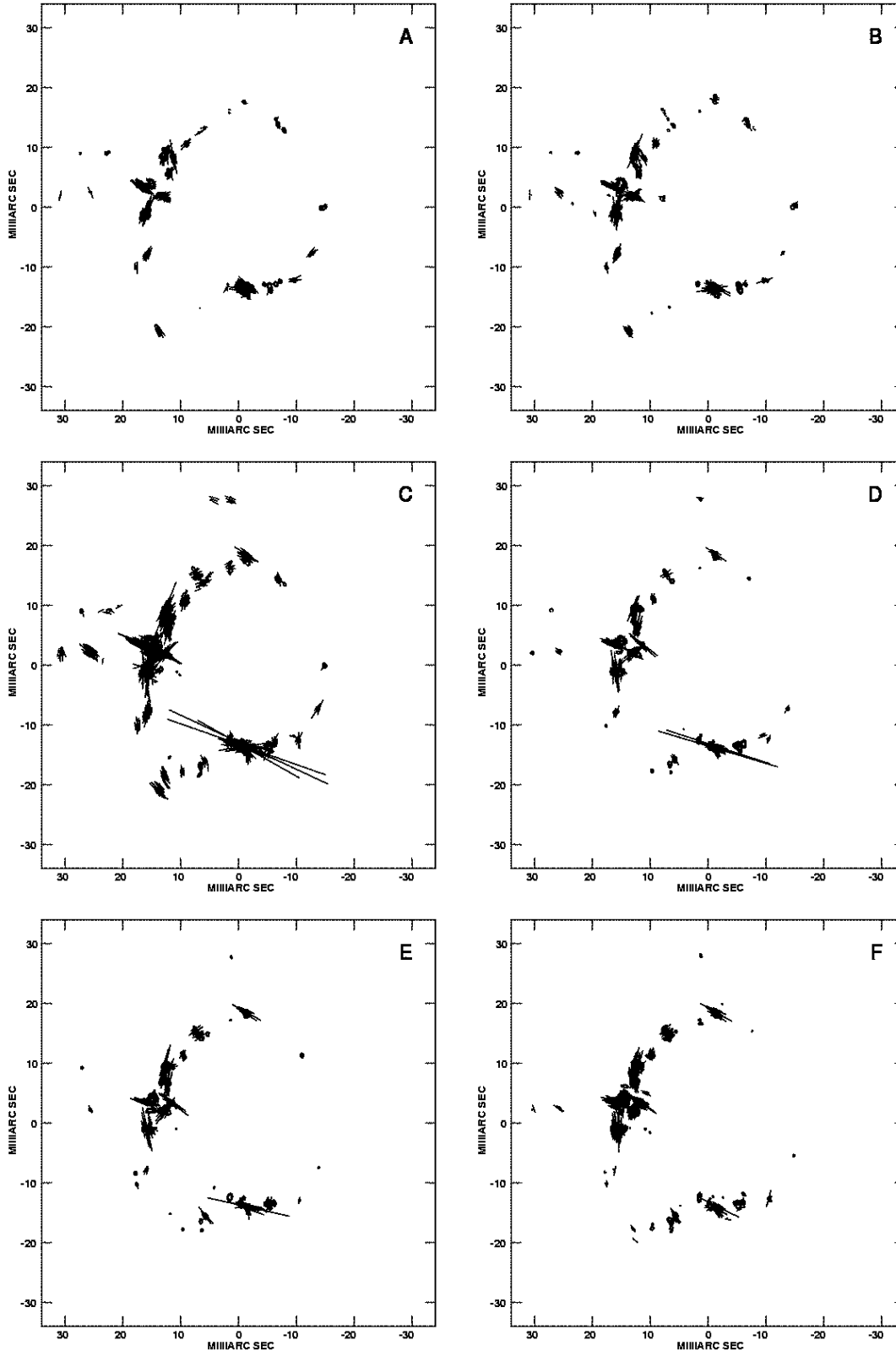


Fig. 3.— For each epoch, a contour plot of the enhanced contrast Stokes I image at levels [1,2,5,10,20,40,80,100] % of the peak. Vectors are overlaid proportional to linearly-polarized intensity (on a scale 10 mas = 18.08 Jy/beam) and drawn at a position angle of the EVPA. All Stokes parameters (I, Q, U) are summed over velocity. The figures are 1360×1360 pixels in size with a pixel spacing of $50\mu\text{as}$. An fixed elliptical Gaussian restoring beam of $540 \times 420\mu\text{as}$ at a position angle of 20 deg was used for all images, representative of the point-spread function for the

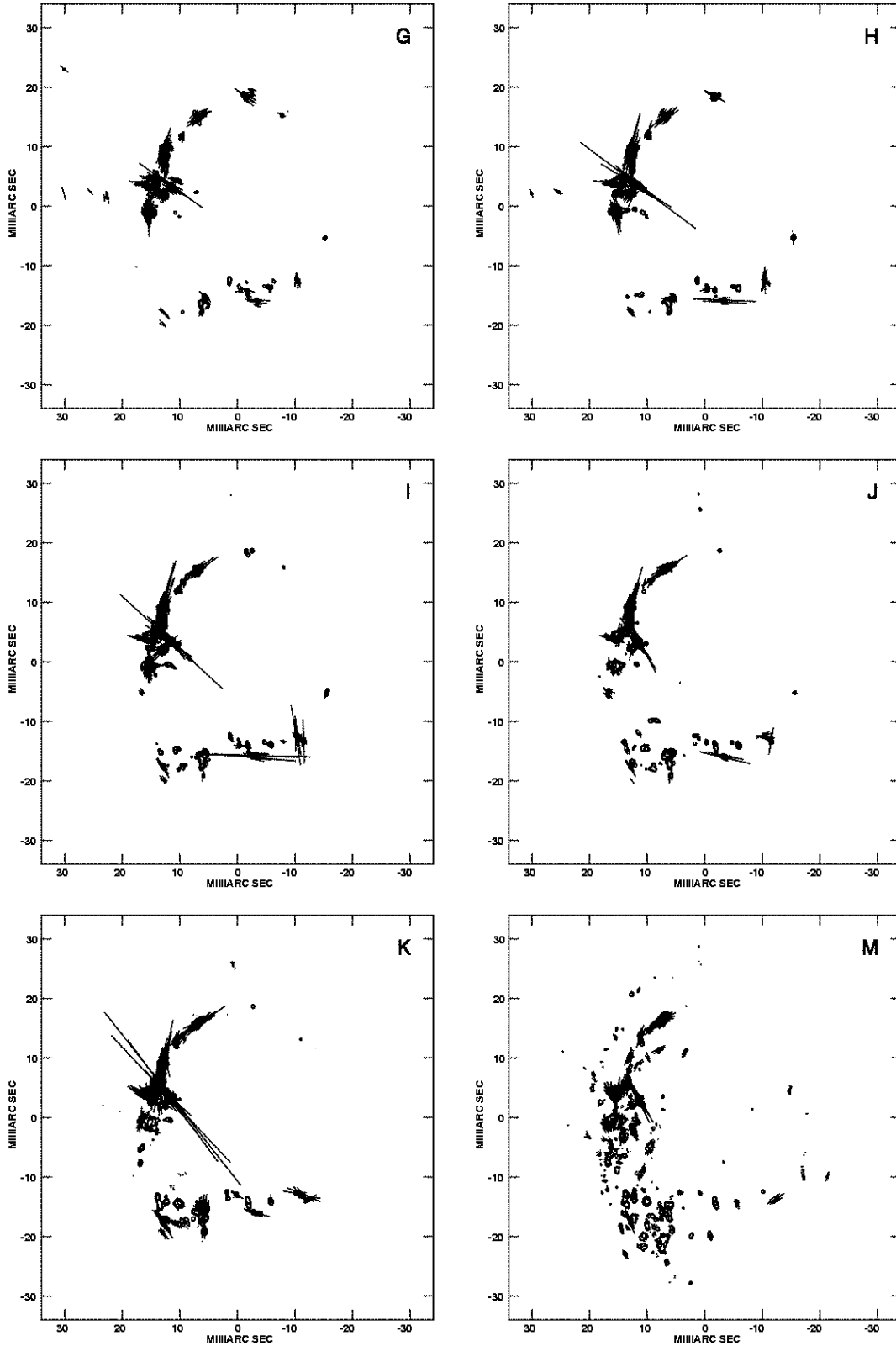


Fig. 4.— Same as Figure 3.

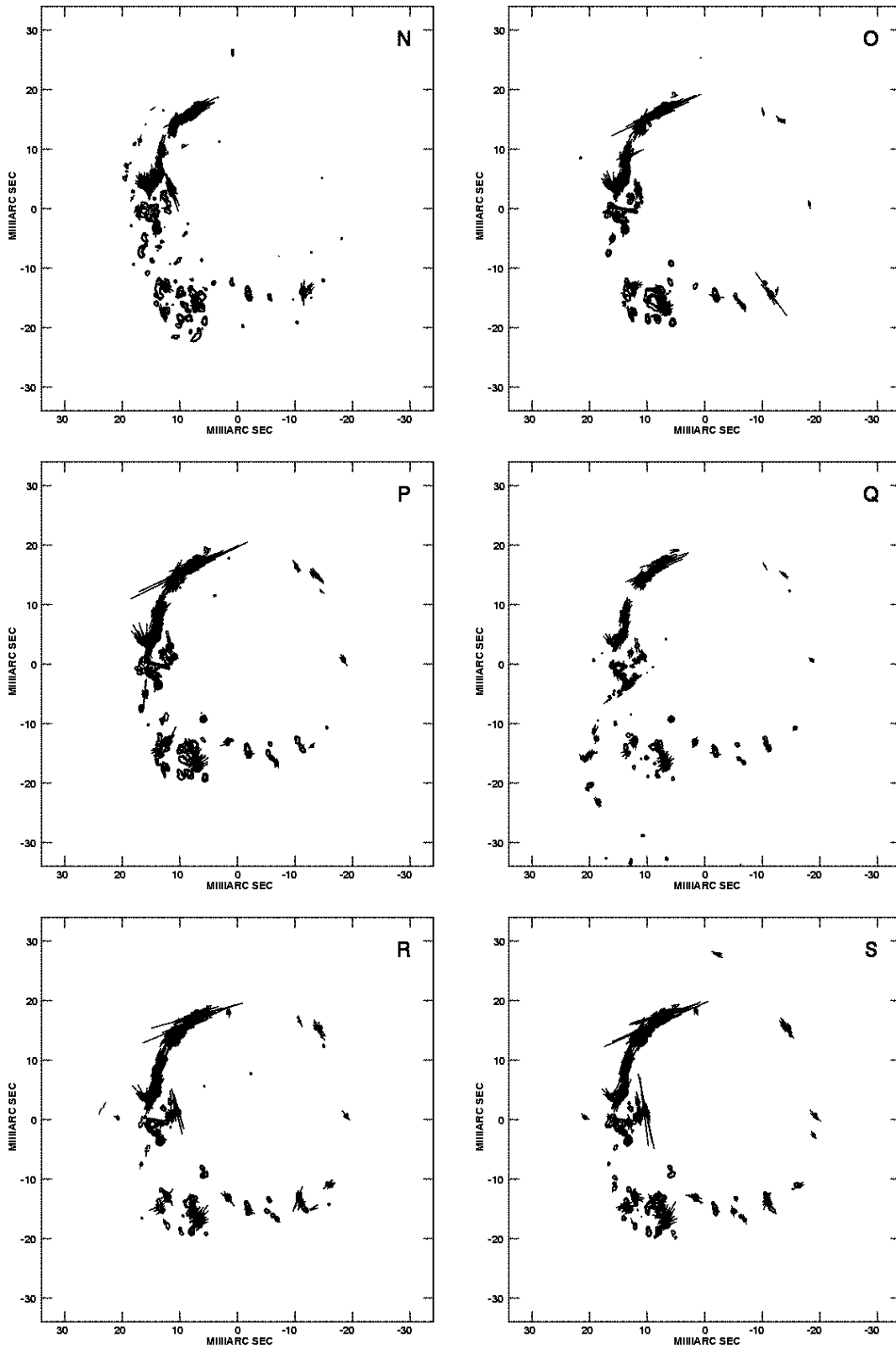


Fig. 5.— Same as Figure 3.

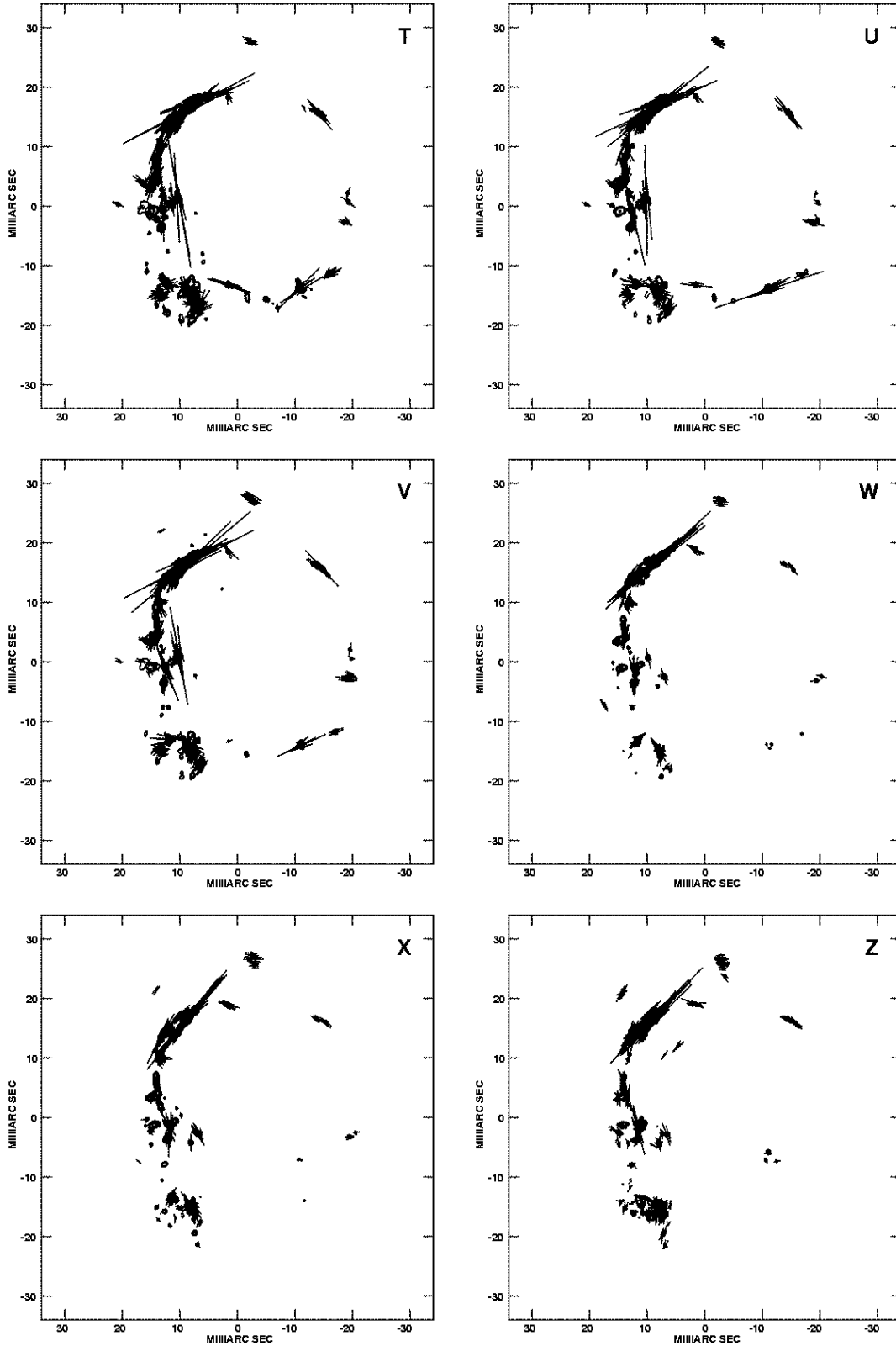


Fig. 6.— Same as Figure 3.

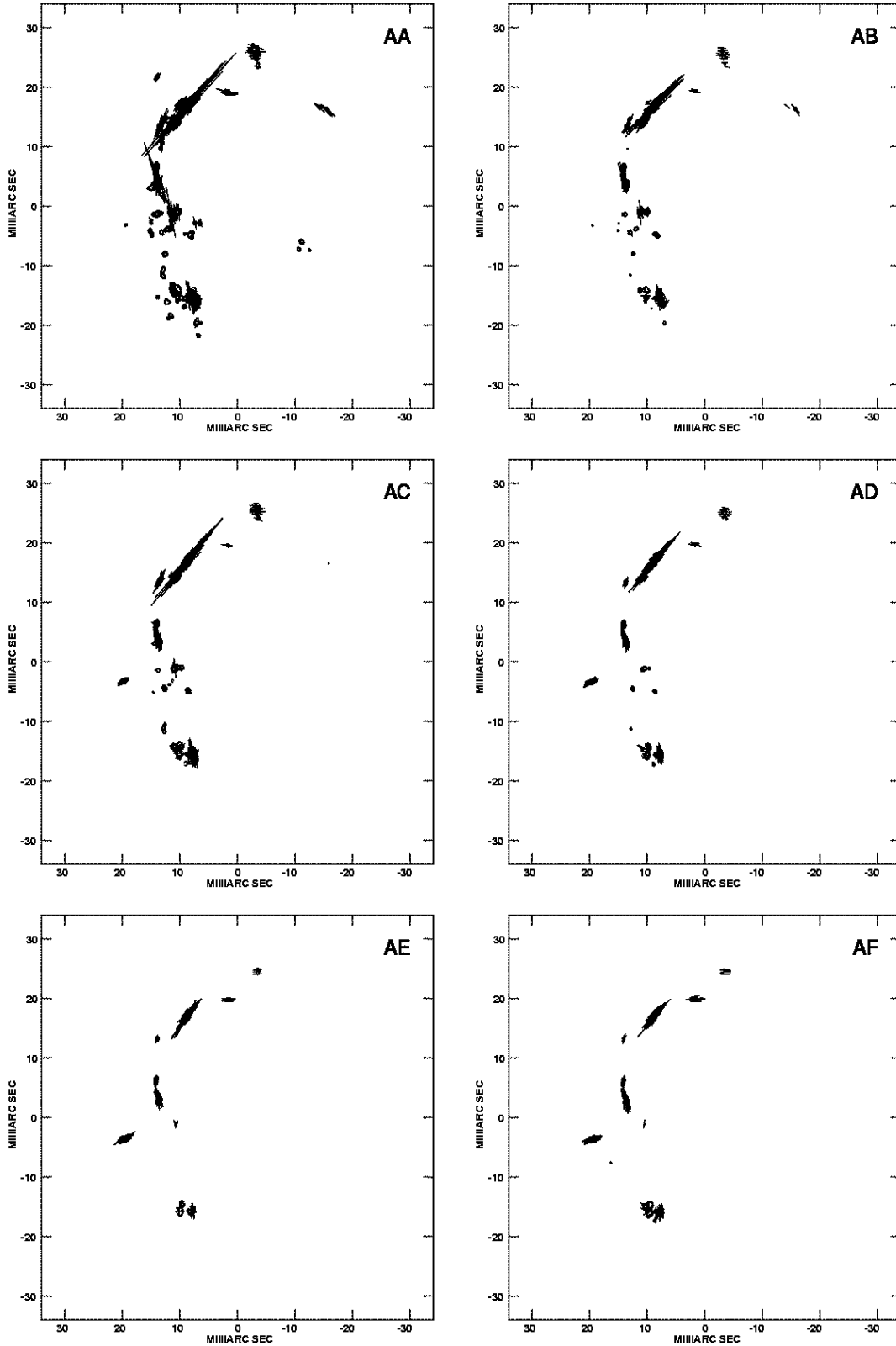


Fig. 7.— Same as Figure 3.

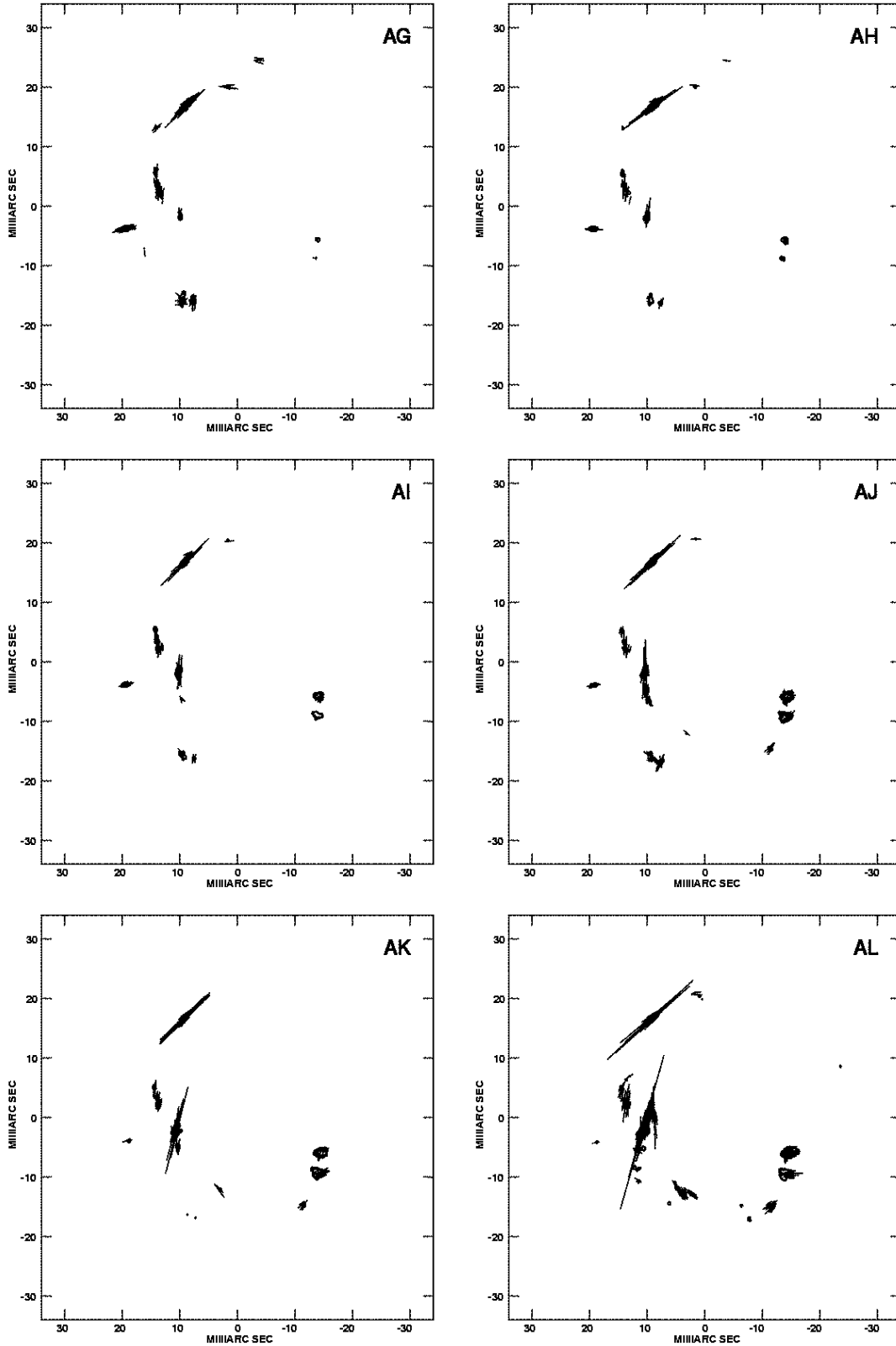


Fig. 8.— Same as Figure 3.

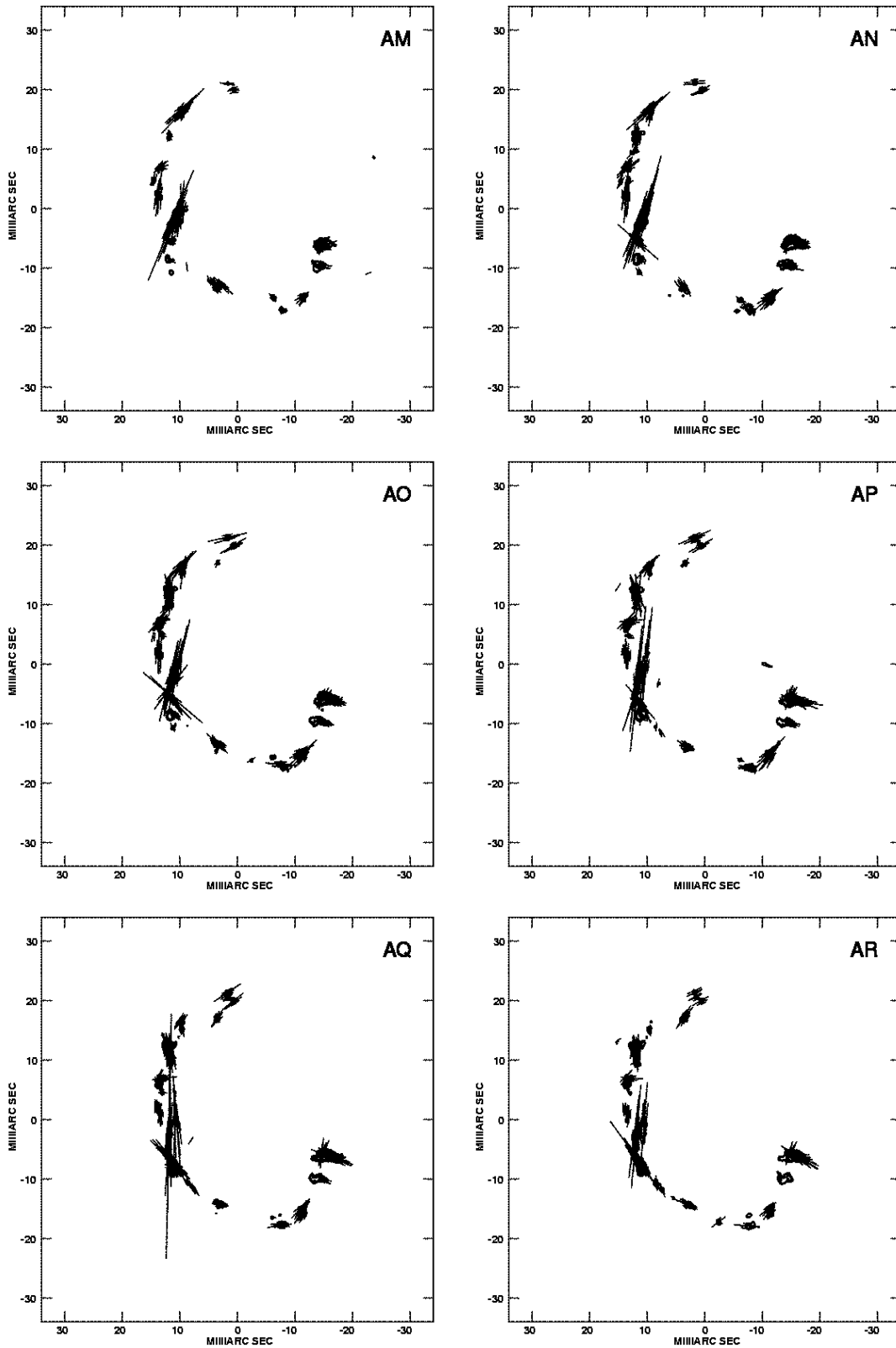


Fig. 9.— Same as Figure 3.

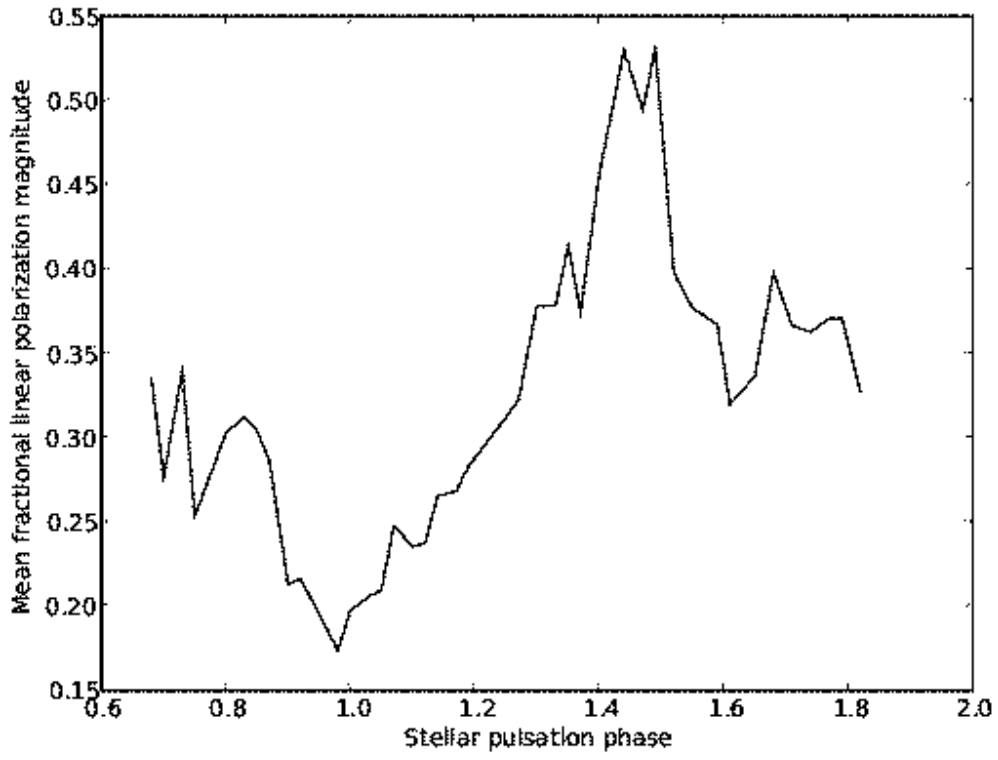


Fig. 10.— The mean fractional linear polarization magnitude as a function of stellar pulsation phase.

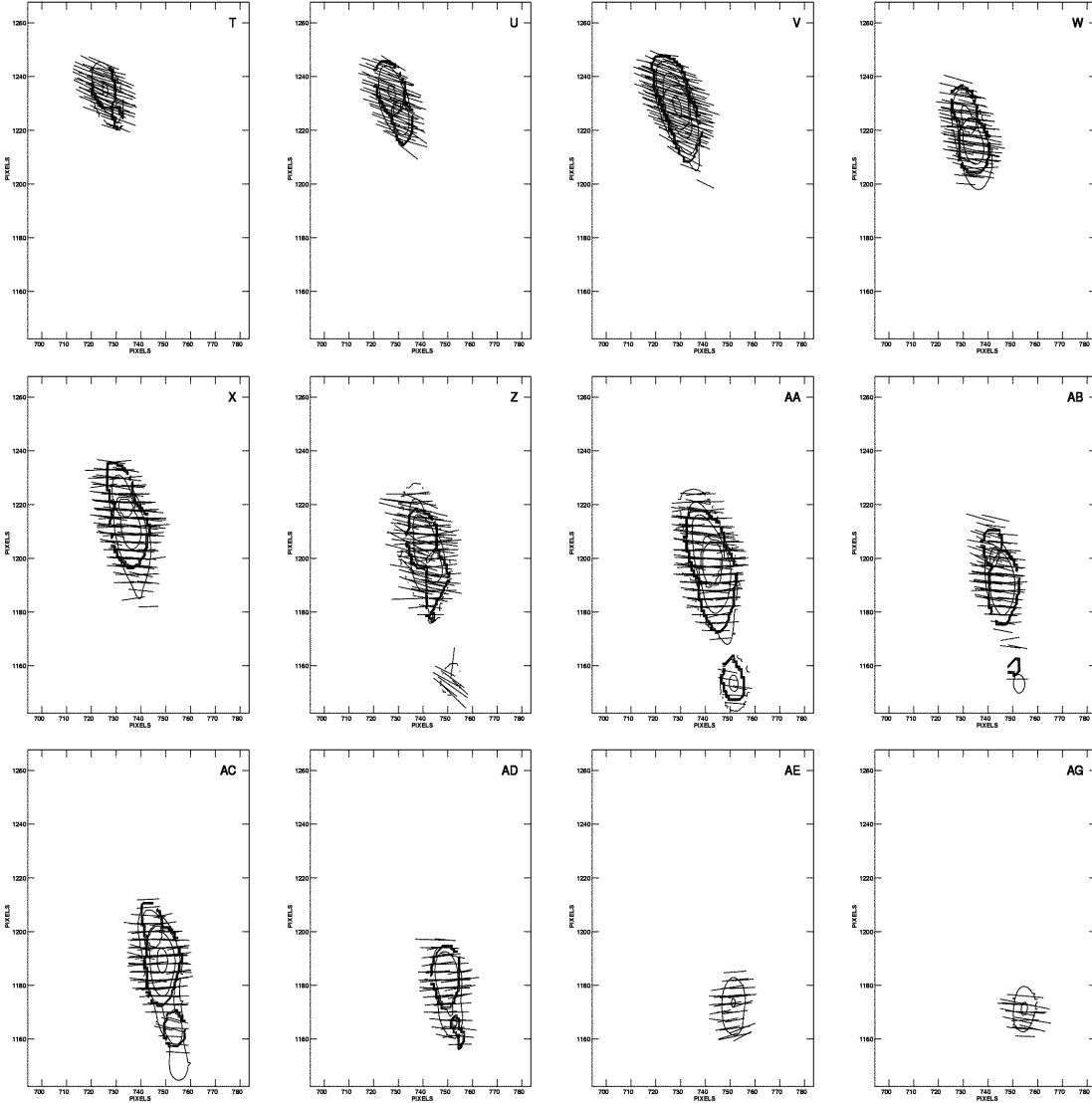


Fig. 11.— A time-series of expanded sub-images of the isolated SiO maser component visible in the far north of images between epochs {S-AH}, falling in toward the northern shell. The plot parameters are the same as for Figure 3, except for a more finely-sampled set of enhanced contrast Stokes I contour levels at $(10^{-1+0.1k}$ for $k=1,30$.)

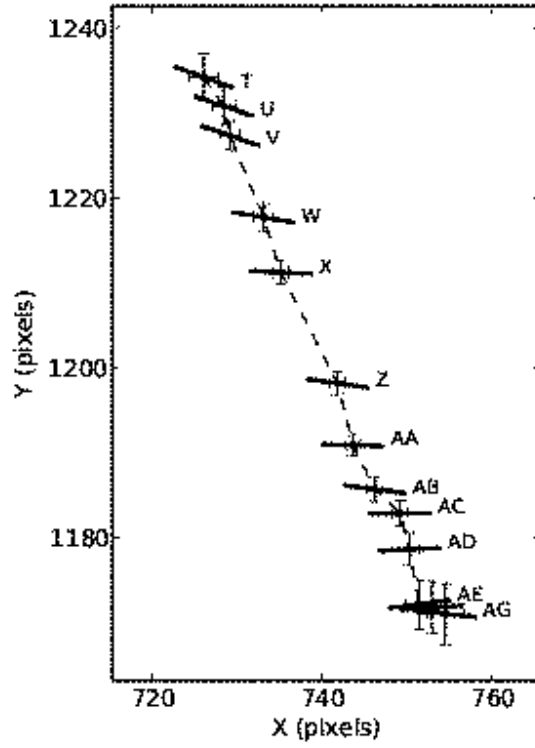


Fig. 12.— A sequence of weighted-mean component positions for the northern component trajectory shown in Figure 11. Error bars in x and y are shown for each weighted-mean position, and the EVPA is drawn at each epoch as a bold vector, of uniform, constant length over epoch.

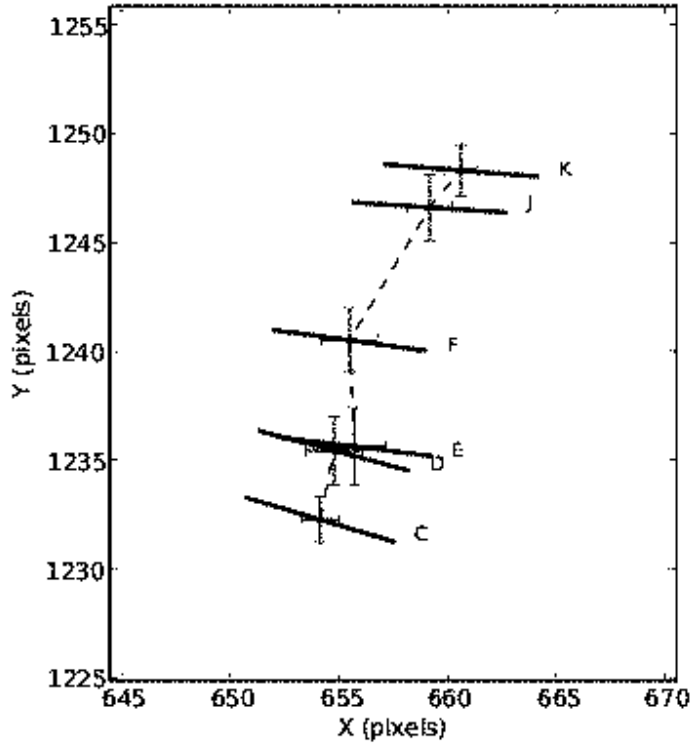


Fig. 13.— A sequence of weighted-mean component positions for the northern-eastern component discussed in the text. Error bars in x and y are shown for each weighted-mean position, and the EVPA is drawn at each epoch as a bold vector, of uniform, constant length over epoch.

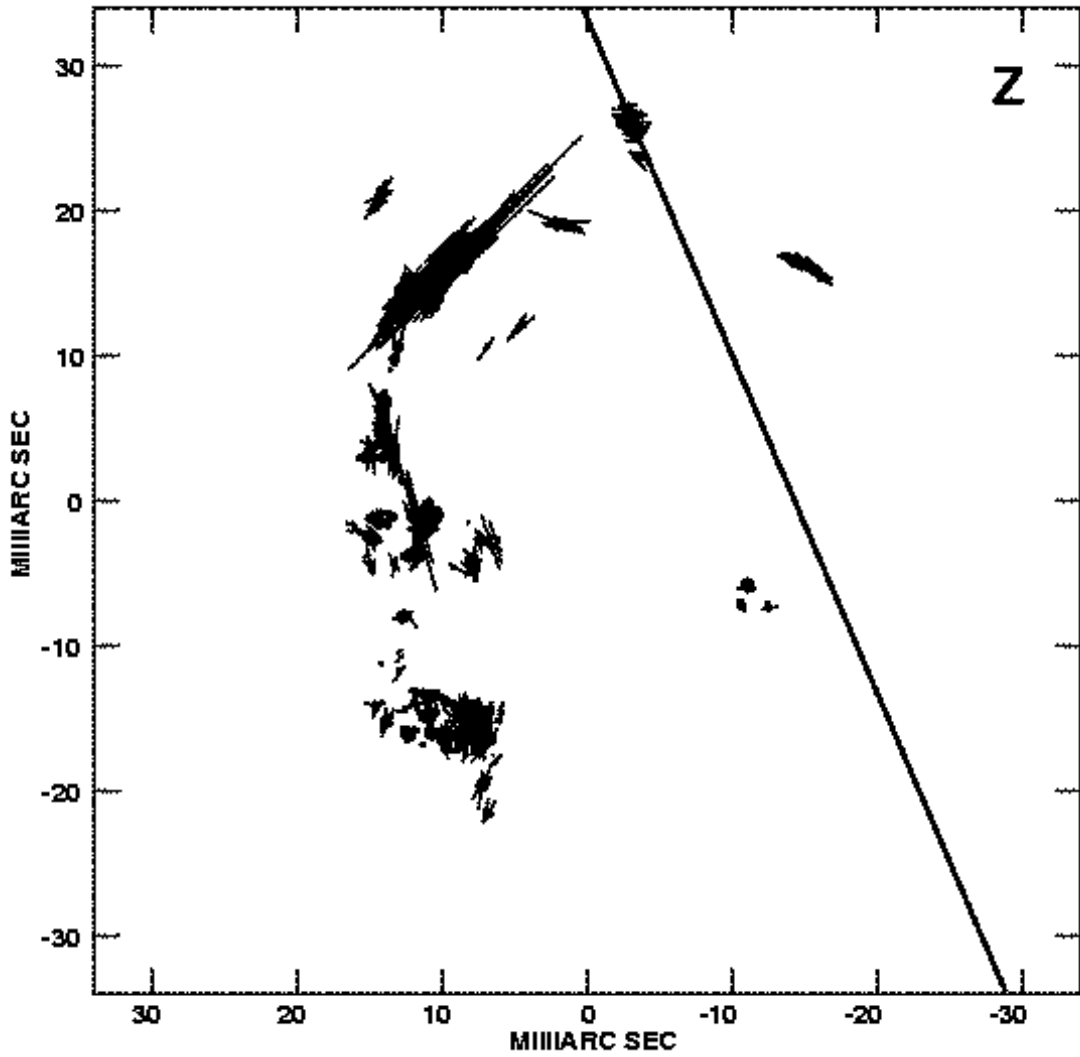


Fig. 14.— The best-fit linear projected trajectory to the northern component positions in Figure 12, extrapolated across the full diameter of the SiO maser shell at epoch {Z}, here chosen as the mid-point epoch of the infalling component trajectory.

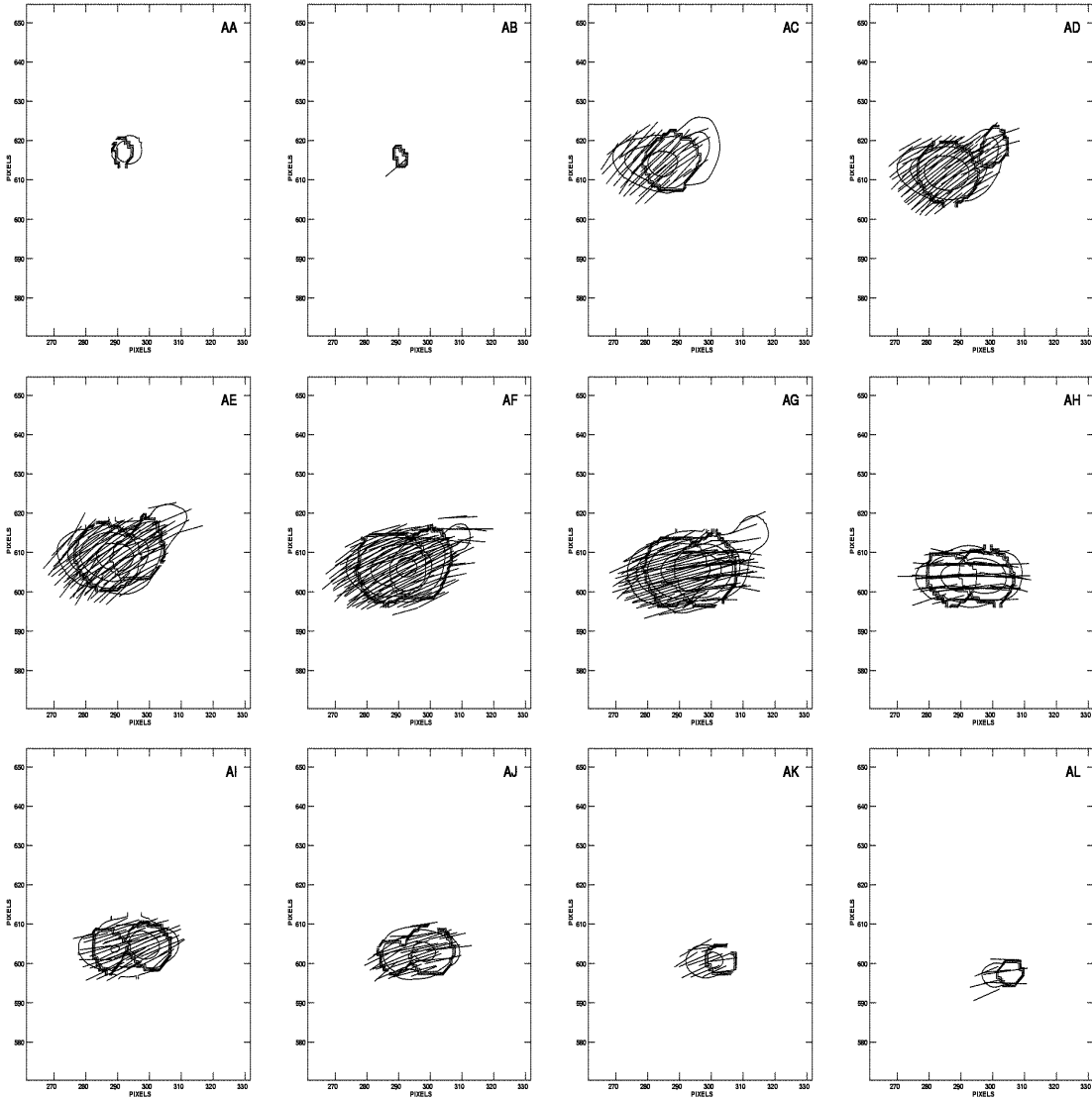


Fig. 15.— A time-series of expanded sub-images of the isolated SiO maser component visible in the eastern part of images between epochs {AA-AL}, falling in toward the eastern shell. The plot parameters are the same as Figure 11.

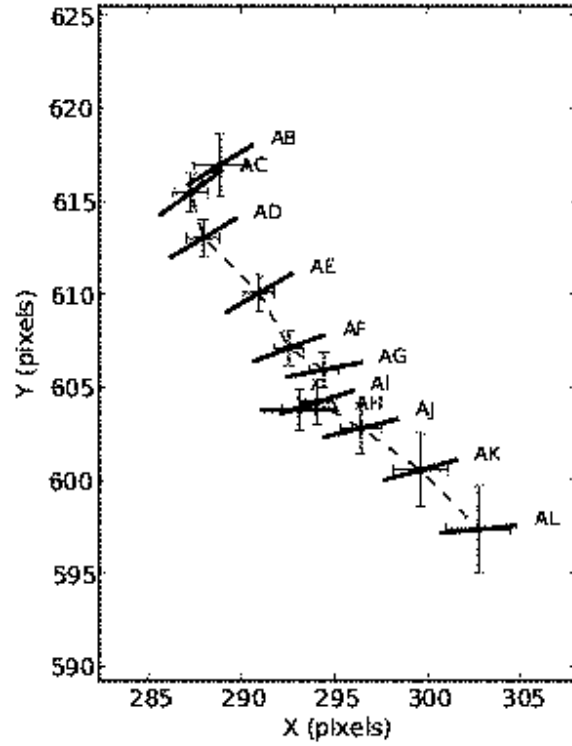


Fig. 16.— A sequence of weighted-mean component positions for the eastern component trajectory shown in Figure 15. Error bars in x and y are shown for each weighted-mean position, and the EVPA is drawn at each epoch as a bold vector, of uniform, constant length over epoch.